UNIVERSITÀ DEGLI STUDI DI PADOVA

Dipartimento di Ingegneria Industriale DII

Insituto Superior Técnico

Corso di Laurea Magistrale in Ingegneria dell' Energia Elettrica

Correlation measurements of the Poloidal magnetic field and plasma potencial fluctuations

Supervisor: Doctor Paolo Bettini
Co-Supervisor: Doctor Artur Louzeiro Malaquias

Luca Cristale 1157066

Anno Accademico 2019/2020

ABSTRACT

This thesis project has been developed at the Instituto de Plasmas e Fusão Nuclear (IPFN) of the Lisbon University on the frame of the plasma diagnostic for fusion. The Heavy Ion Beam Diagnostic HIBD is a diagnostic tool operating on the ISTTOK tokamak. The present ISTTOK-HIBD configuration measures three different plasma parameters: plasma pressure-like $n_e\sigma(T)$, poloidal magnetic field (B_p) and Plasma potential (V_p).
The poloidal magnetic field (B_p) measurement is correlated to the toroidal Shift on the Front Multiple Cell Array Detector (MCAD) while the Plasma potential (V_p) is correlated to the toroidal Shift on the Back MCAD of the 90^0 Cylindrical Analyzer (CEA), an hardware component of the HIBD for the V_p measurements.
The thesis project describe the routine of a Matlab program for HIBD Data processing and analysis. The program Data Analysis routine computes an approximate value of Ion Beam Current passing through a slit on the front detector. Comparing this values with the ion beam current detected on the Back MCAD was possible to measure an estimation of the beam current lost inside the Electrostatic Input Module (EIM) $[45 - 50\%]$, the EIM is an hardware component of the HIBD that separate the Front MCAD from the CEA.
The program Data Analysis routine also computes and cross-correlates the toroidal shift on Front and Back MCADs demonstrating that there is not cross-talk between the two Signals (normalized cross correlation range r_{xy} $[-0.2 \ + 0.2\%]$) so that there is no interference between B_p and V_p measurements.

ACKNOWLEDGEMENTS

I would like to start by thanking my co-supervisor, Prof. Artur Malaquias, for his support during the execution of this work, for his advices and corrections. For all the direct and indirect motivations he gave me for reasoning with independence on problems and solutions that a research work daily requires.

I would like to thank my supervisor Paolo Bettini for the opportunity he gave me to experience a period of work in a foreign frame, living in a research environment that gave me the possibility to mature new personal and job skills.

I would like to express my gratitude to Dr. Ridhima Sharma, her patience, kindness and experience helped me every day in dealing with all the theoretical and practical knowledges that were new for me.

Voglio infine ringraziare i miei genitori, supporto emotivo e materiale di tutta la mia vita.

CONTENTS

LIST OF FIGURES

LIST OF TABLES

1

FUSION ENERGY

1.1 CONTEXT

The access to affordable, abundant energy, mainly from fossil fuel sources, has been a key factor of economic growth since the Industrial Revolution [7], but the increase in the world energy demand and the awareness of the correlation between CO_2 emissions and global warming stimulates the scientific research to investigate different energy distribution methods and green production technologies.
Several renewable sources have been implemented to the electric power production system: solar, hydro, wind and others. It is expected that they will play a key role in the management of the environmental problem, but they won't represent the unique and ideal solution. Renewable sources depend on the morphological, geological and climate characteristics of the area and, consequently, the production of electric energy may be discontinuous (solar , wind and others) or saturable (hydro and others). Moreover they require the development of more suitable electric transmission systems because the renewable sources are not involved to the balance of the grid frequency, a fundamental aspect of the electric energy transmission.
Nuclear fission doesn't emit CO_2 but require long-life radioactive storage systems, moreover it may involve geopolitical issues due to the possible proliferation of nuclear weapons.
The controlled thermonuclear fusion represent currently a promising technology for a long lasting large-scale energy source. A future nuclear reactor will not emit CO_2, it will be intrinsically safe with respect to fission because it will not involve chain reactions and it won't be used to produce nuclear weapons. Currently the nuclear fossil fuel consists of Deuterium (D) and Tritium (T). Deuterium can be extract from the sea water while Tritium from lithium, so the fuel limit is represented by the lithium resources that are abundant on earth's crust, hence fusion may guarantee many centuries of electric energy production.

1.2 FUSION REACTION

Fusion is a form of nuclear energy that involves the merging of light elements to form a nucleus with a larger mass number.
The nucleai of atoms are constituted by protons (Z) and neutrons (N=A-Z, where A is the atomic mass of the element), but the mass of a nucleus is always less than the sum of the single masses of its protons and neutrons. The difference represents the nuclear binding energy, which holds the nucleus together.
The energy released during a fusion reaction indicates an increase in the binding energy of the nuclei between the final and the initial states. At the end of the reaction, the rise of the binding energy corresponds to a decrease in the

final total nuclear mass. This difference in mass is transformed into energy following Einstein's equation 1.1:

$$E = \Delta mc^2 \tag{1.1}$$

There are different reactions that might be interesting to produce fusion energy but the one that has gained more interest from the scientific world involves the combination of an atom of Deuterium with one of Tritium, as following 1.2:

$${}^2_1H + {}^3_1H \rightarrow {}^4_2He + {}^1_0n + 17.59MeV \tag{1.2}$$

Among all the possible fusion reactions, this one (1.2), also named as D - T reaction, is the easiest fusion reaction to initiate since it can be carried out at lower temperatures, like 150 - 200 million °C. The D - D reactions are the following (1.3 and 1.4):

$${}^2_1H + {}^2_1H \rightarrow {}^3_2He + {}^1_0n + 3.27MeV \tag{1.3}$$

$${}^2_1H + {}^2_1H \rightarrow {}^3_1H + {}^1_1H + 4.04MeV \tag{1.4}$$

As a matter of fact, the Deuterium - Deuterium reaction (D - D), which is another possible fusion reaction, requires higher temperatures (400 - 500 million °C) since there is a lower probability that a pair of D - D nuclei will collide. Figure. 1.1 compares the cross-section of three different possible reactions at different energy.

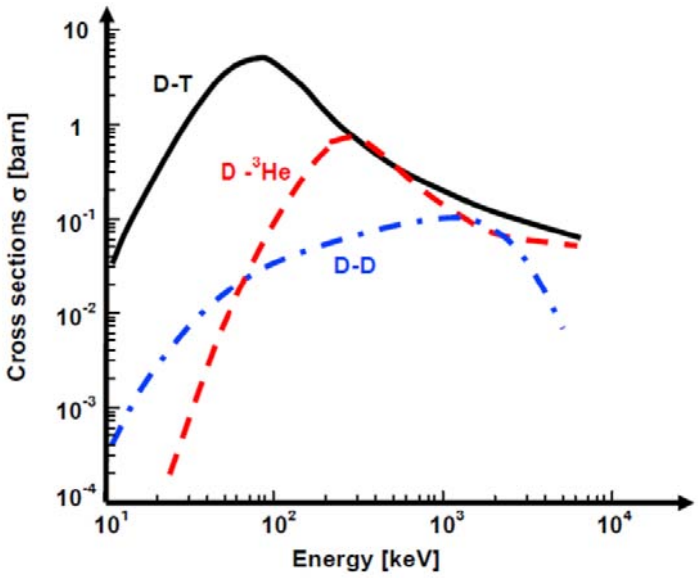

Figure 1.1: *Measured cross sections for different fusion reactions as a function of the averaged center of mass energy. Reaction cross sections are measured in barn*

All fusion reactions can occur only if the interacting nuclei have kinetic energy that overcomes the repulsive Coulomb potential energy. If not, the two nuclei will drift away from each other before they collide. To provide the amount of energy necessary to overcome the Coulomb barrier the reactants

are heated to very high temperatures, in order to rich a plasma state. This can be defined as a partially-ionized gas containing ions, electrons, and neutral atoms. In a plasma, some electrons are freed from their atoms, allowing current and electricity to flow.

Taking into consideration the Deuterium-Tritium reaction (1.2), the Deuterium, which is one of the reactants, can be distilled from water. Therefore, it can be considered as a harmless, very available and inexhaustible resource. By contrast, the second required fuel, which is Tritium, is a fast-decaying radioelement of hydrogen that can only be found in small quantities in nature. To overcome this issue, Tritium is breed in the blanket surrounding the region of D - T reaction and it is produced during the fusion reaction from lithium: neutrons that escape from plasma interact with lithium contained in the blanket wall of the reactor and tritium is produced by the following reaction 1.5:

$$ {}^{6}_{3}Li + {}^{1}_{0}n \rightarrow {}^{3}_{1}H + {}^{4}_{2}He + 4.78MeV \tag{1.5} $$

Taking into consideration both reactions 1.2 and 1.5, an overall reaction 1.6 can be derived:

$$ {}^{2}_{1}H + {}^{6}_{3}Li \rightarrow 2\ {}^{4}_{2}He + 4.78MeV \tag{1.6} $$

The latter demostrate that Deuterium and Tritium constitute the fuel for fusion.

On Earth, the way to achieve D-T fusion reactions is to create a hot plasma characterized by specific conditions of density, temperature and duration in time.
To satisfy these conditions, two main types of fusion confinements exists: magnetic and inertial. The inertial confinement fusion (ICF) consists of compressing and heating a D-T frozen pellet by using high-energy laser beams. The magnetic confinement fusion (MCF) consists of confining the D and T ions with magnetic fields while providing heat via other additional sources. The point where the reaction is self-sustained without providing external heating for a power-producing thermonuclear fusion reactor is called ignition, J. D. Lawson established a criterion to reach it: here reported in terms of triple product, considering a plasma of Deuterium and Tritium:

$$ nT\tau_E \geq 1.2 \cdot 10^{21} \quad [m^{-3}keVs] \tag{1.7} $$

where [n] is the plasma density, [T] is the Temperature and τ_E is the energy confinement time, which indicates the rate at which the system loses energy to the environment. To wrap up, in order to produce energy from fusion reactions, a sufficiently hot (T) and dense (n) plasma must be confined effectively (τ_E) Assuming a 50% mixture of Deuterium and Tritium the minimum product of $n\tau_E$ factor, in practice, is obtained at temperature T close to $\sim 10keV$.
The power gain by the reactor is given by:

$$ Q = \frac{P_F}{P_H} \tag{1.8} $$

where P_F is the power generated by the fusion reaction and P_H is the heating power. By definition the ignition condition is obtained for $Q \rightarrow \infty$, (i.e for $P_H = 0$) that is not a practical condition, a reactor has to reach a power gain factor close to $Q \sim 10$

1.3 TOKAMAK

Among the three main MCF device configurations: tokamak, stellarator and reversed field pinch (RFP), the tokamak is currently the most promising configuration for a future nuclear fusion reactor. These configurations consist of a toroidal ("donut") shaped device. When comparing to a tokamak, one of the main disadvantages of a stellarator is its complexity to build from the engineering point of view (not toroidally symmetric) while one of the RFP main limitations as the future reactor is the pulsed operation due to the need of high plasma currents.
The present-day largest tokamak in operation is the JET at Culham (CCFE), United Kingdom. The planed steps to the realization of fusion electricity are described by the *European roadmap* into eight missions. For each mission, it reviews the current status of research, identifies open issues, and proposes a research and development programme. ITER is the experimental power plant that is under construction in Cadarache (France) and represent the key facility on the roadmap as it is expected to achieve most of the important milestones on the path to fusion power. The Fusion Roadmap is tightly connected to the ITER schedule and the vast majority of resources in fusion research are presently dedicated to ITER and its accompanying experiments. Parallel to the ITER exploitation in the 2030s, the construction of the demonstration power plant DEMO needs to be prepared. DEMO will for the first time supply fusion electricity to the grid and it will have a self-sufficient fuel cycle. The design, construction and operation of DEMO require full involvement of industry to ensure that, after a successful DEMO operation, the industry can take responsibility for commercial fusion power. [8]

1.3.1 *Plasma Confinament*

Since any material would melt in contact with the extremely hot fuel, the plasma must be prevented from touching the walls of the confinement chamber. This confinement method is based on the constrained motion of the charged particles of the plasma by a magnetic field.
A charged particle can move freely along magnetic field lines, but its movement perpendicular to the field lines is restricted due to the Lorentz force ($F = qv \times B$, where q is the charge of the particle, v the particle velocity and B the magnetic field) acting on charged particles like the positively charged nuclei and negatively charged electrons that form the plasma. The Lorentz force guides the particles to move perpendicularly to the magnetic field into circular motion around a magnetic field line resulting in gyrating particle orbits with a finite radius, the Larmor (or gyro) radius: $rL = mv_{\perp} / |q \mid B$, where m is the particle mass, $v_{\perp}$ is the particle component velocity perpendicular to the magnetic field (B).
The curvature of the toroidal field introduces forces on the plasma that cause particle drifts and eventually disruption of the plasma. The particles tend to drift away from the magnetic flux surfaces due to mechanisms arising from the electromagnetic fields. One of them, the so-called *gradient B drift*, is caused by the radial gradient in the magnetic field due to the compression of the field lines on the inside of the torus. For a charged particle the gyration radius varies with the magnetic field strength, resulting in a minimum on the high field side HFS (the inner side of the torus) and a maximum on the low field side LFS (the outside). This causes the particle to drift in the vertical direction. Because the ions and the electrons gyrate anti-parallel to each other

they also have different drift directions, creating a charge separation with an associated electrical field.
To counteract the drift effect, the magnetic field is given a poloidal component by driving current in the plasma. The magnetic field lines then follow a helical path around the torus, thus cancelling the vertical drifts. A stable plasma equilibrium can be reached by twisting the magnetic field lines by superimposing toroidal and poloidal field components. Magnetic field lines wrap around the torus axis in a helix and constrain the path of the charged particles in the fuel. In a tokamak, the toroidal component B_p is generated by poloidal magnetic coils that are wound around the torus. Fig. 1.2 shows a schematic view of the tokamak concept.

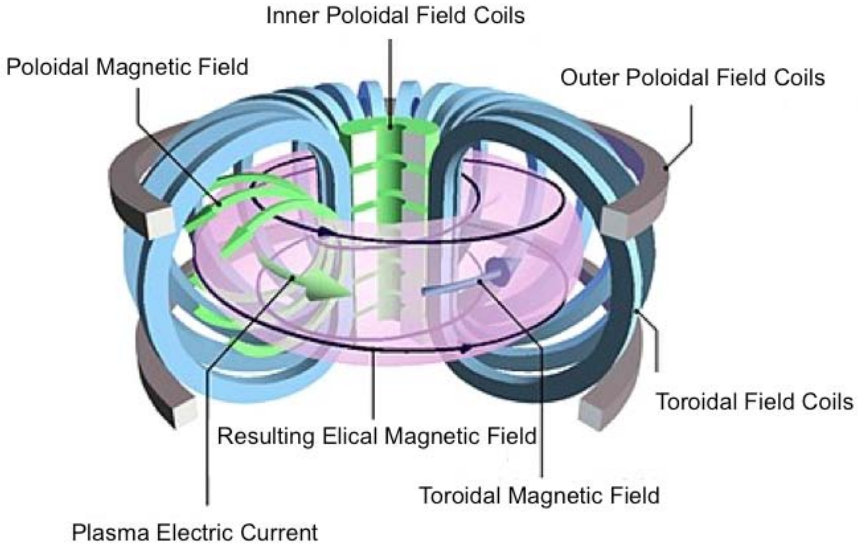

Figure 1.2: *Schematic tokamak rapresentation*

The poloidal field is more complex to produce since the toroidal current must flow inside the plasma. A straightforward way to create a poloidal magnetic field is by using the plasma as a secondary circuit in a transformer, with poloidal coils surrounding the plasma. In this setup, the plasma acts as a single secondary loop generating the poloidal magnetic field. The plasma itself, which is an excellent electric conductor, is the secondary loop, and so has a large current induced in it. This plasma current produces heat, just as a wire warms up when an electric current flows through it.
To have a plasma in equilibrium, centred and with the desired shape, some extra fields not shown in Fig. 1.2 are necessary. These fields are created by the combination of external toroidal (poloidal field) coils. At the densities and temperatures reached in fusion plasmas, significant kinetic pressure is obtained in the plasma core and large pressure gradients produce strong forces on the plasma. The ∇p forces are balanced by $j \times B$ forces arising from the magnetic field interacting with toroidal and poloidal plasma currents. This force balance is often called the magnetic equilibrium of a plasma configuration. [9]

1.3.2 *Additional heating and current drive*

The resistance of the plasma current inside the vacuum chamber decreases with the temperature as $T^{-\frac{3}{2}}$. where Te is the electron temperature. This means that at the beginning of discharge, Ohmic heating is a convenient heating method, but at higher temperatures the the heating method becomes inefficient and additional technologies must be implemented, e.g. neutral beam injection (NBI) or resonant interaction between particles and electromagnetic waves such as the electron cyclotron (EC) wave, the ion cyclotron (IC) wave, the lower-hybrid (LH) wave, etc. Both NBI and radio-frequency (RF) wave injection are the non-inductive heating method that can sustain a steady-state plasma. In NBI high energy neutral particle beams are injected into the plasma to transfer their energy to the plasma ions. By accelerating ions with high voltage that are converted into neutral atoms just before the injection the particle beam is generated. Charged particles orbits in a tokamak are characterized by three periodic motions and their respective frequencies: the gyro-frequency for the rotation around field lines, the bounce- or transit frequency for the parallel motion along the field lines, and the drift frequency. By appropriately choosing the frequency and the launching characteristics of RF waves, it is possible to control the resonant interaction of these waves with electrons or ions. Particles of specific species and characteristics (location, energy, magnetic moment) can thus be targeted by controlled RF heating. [9]

1.3.3 *First Wall and Plasma-Facing components*

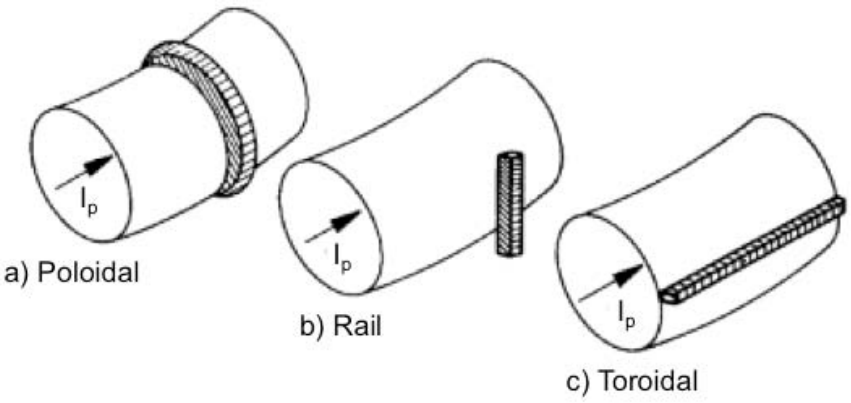

Figure 1.3: *Schematic representation of different types of limiters, courtesy from A. Pezzoli [1]*

The PFCs are those systems directly facing thermonuclear plasma: they are generally said to constitute the so-called first wall. They must operate in a very harsh environment while maintaining their functional properties. It is possible to define the following main components:

Limiter Fig. 1.3: is one of the candidate structures for sustaining the Plasma Material Interaction (PMI) together with the divertor (described properly be-

low). A limiter is a solid surface that protrudes from the blanket toward the plasma region. It can run along the vacuum vessel (toroidal limiter) or along the poloidal section (poloidal limiter) or be localized in a precise area of the vacuum vessel (rail limiter). Schematic examples of possible limiter configurations are reported in Fig. 1.3. In the case of limiter configuration, the Last Closed Flux Surface (LCFS) corresponds to the limiter solid surface and consequently impurities generated by the limiter are injected directly into the plasma region. [1]

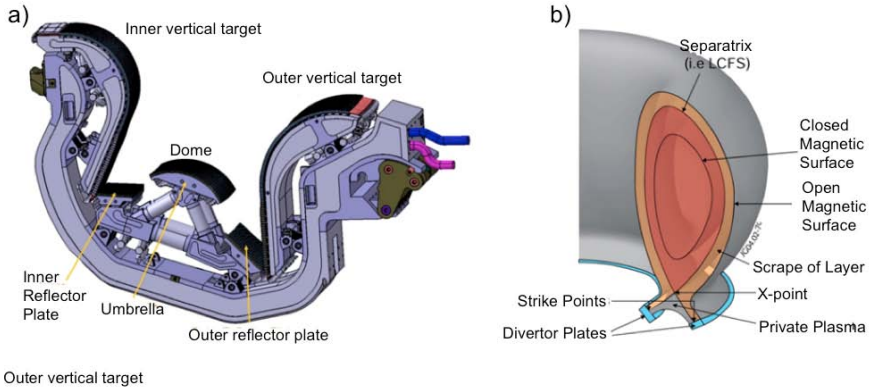

Figure 1.4: *a) ITER divertor design. (b) Geometry of a toroidal magnetic field with divertor, courtesy from A. Pezzoli [1]*

Divertor solution is used to solve this problem in the limiter case. In divertor configuration the outer poloidal field lines are open and directed towards toroidally symmetric regions named divertor target plates Fig. 1.4 . This solution performs better than the limiter option and, in particular, makes it possible to have high confinement plasma regime (H-mode) . The divertor system must withstand the highest thermal loads and particle fluxes in the tokamak and for these reasons, its design and the choice of materials are fundamental for guaranteeing that the tokamak will work properly. Nevertheless, it is crucial to note that it is possible to protect the divertor form these phenomena if the plasma is detached. This means that plasma has a high density and low temperature in the divertor region.

Blanket has the fundamental role of protecting the toka- mak's structure and coils from thermonuclear plasma (e.g. thermal loads, neutron flux, particles flux, etc.). [1]

2

EXPERIMENTAL SET-UP

Chapter 2 presents the experimental set-up, it is composed of two main sections. The first section describes the electrical, dimensional and operational characteristic of the experimental tokamak ISTTOK while the second section describes the functional principles, hardware components characteristics and measurements principles of the Heavy Ion Beam Diagnostic (HIBD).

2.1 ISTTOK TOKAMAK

ISTTOK (IST + TOKamak) is a tokamak in operation since 1993 at *Centro de Fusao Nuclear (CFN)*, in the frame of the Fusion Programme of the European Atomic Energy Community (EURATOM). Its construction was started in mid-1990 reusing some components of the former TORTUR tokamak (support structure, vacuum vessel, copper shell, toroidal magnetic coils, transformer, capacitor banks, radiofrequency generator and discharge cleaning system). The other components of ISTTOK (vacuum and gas injection systems, poloidal windings and power supply for the toroidal B field) as well as its diagnostics and control and data acquisition system was on-site designed and built [10].

2.1.1 *Tokamak parameters*

ISTTOK is a small size tokamak with a circular cross-section, large aspect ratio and an iron core transformer. The vacuum vessel is surrounded by a copper shell (15 mm thick) to allow for passive stabilization of the plasma.

The geometrical and electrical ISTTOK parameters are shown in Table 2.1

Parameters	Value
Major Radius	0.46 m
Minor Radius	0.085 m
Toroidal Magnetic Field	0.5 T
Transformer Flux	0.25 Vs

Table 2.1: *Geometrical and Electrical Parameters*

The Plasma operation is in AC mode and the gas used on the thesis experimental set-up is Hydrogen but also Deuterium and Helium can be adopted. The main Plasma parameters are shown in Table 2.2

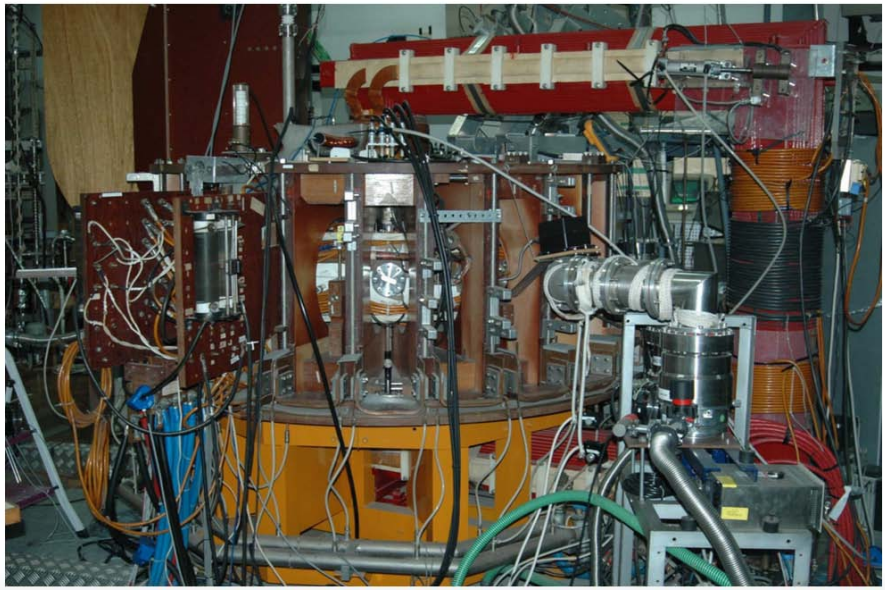

Figure 2.1: *Photograph of ISTTOK tokamak highlighting the transformer core (red) and toroidal field coils (vertical)*,courtesy from H. Fernandes [2]

Plasma Parameters	Value
Current	4 kA
Line Density	$4 \cdot 10^{18}$ m
Temperature	< 120 eV

Table 2.2: *Plasma Parameters*

2.1.2 *Operation*

A peculiar characteristic of the ISTTOK tokamak is the AC operation mode. AC operation consists of alternating the plasma current between positive and negative directions. Inverting the plasma current prevents reaching the transformer swing limits and allows for a quasi-steady state or almost continuous operation. In this case, the energy production, occurring at the high-performance plasma phase, is only interrupted for a small period of time (dwell time) corresponding to the time of the current inversion: ramp-down and ramp-up. The dwell time is usually much smaller than the high power phase time. If the current inversion is performed fast enough, the ionization is not lost and the transition is performed with a non-zero plasma density even at $I_p = 0$. In the typical experimental condition, each cycle lasts at 50 ms, with the positive cycle holding approximately up to 35 ms.

2.1.3 *Power Supplies*

Discharges in both directions with similar durations and symmetric plasma currents were obtained applying symmetric voltages to the primary of the transformer, with the same toroidal B-field. This means that the power supplies must also be invertible. The power supplies were built aiming to provide the fastest reaction time possible with stable output, in such a way to

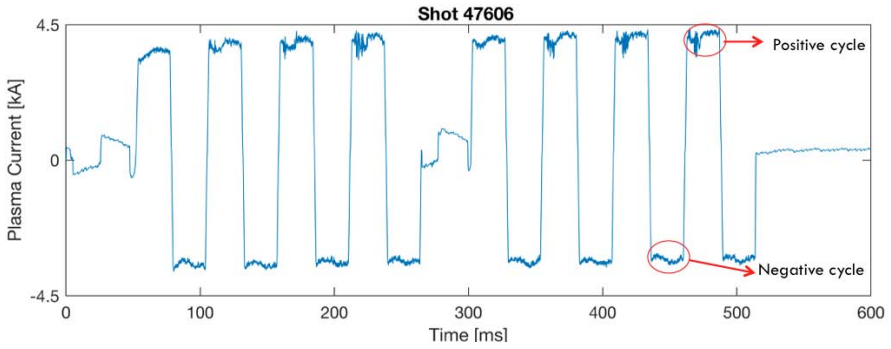

Figure 2.2: *AC operation at ISTTOK with plasma current range* $[-4\ 4]$ *kA and acquisition time range* $[0\ 600]$ *ms*

allow the stabilization of the plasma position as fast as possible. [11] ISTTOK power supplies are three and they respectively control the i) ohmic field generated, ii) the vertical field generated by 2×6 windings placed close to the inner surface of the toroidal coils and the iii) horizontal field generated by 2×6 windings wrapped over the copper shell [12] [13]. A summary of the power supplies specifications can be found in Table 2.3.

Power supply	Limits
Horizontal field PS	$\pm$150 A
Vertical field PS	$\pm$450 A
Magnetising field PS	$\pm$350 A

Table 2.3: *Power supplies maximum current*

The power supplies have their own independent current feedback control and communicate by means of an optical link with the main control system at a rate of 921.6 kbit/s. The power supplies current controller has a 34.6 s control cycle running on a $DSPIC30F2020$ [11]

2.1.4 *Acquisition and Control Systems*

The control system is a solution that enables us to control and operate all the machinery in very small scales of time and/or operates it for long periods of time. The ISTTOK CODAS (COntrol and Data Acquisition System) consists of two control subsystems: slow and fast; and two data acquisition (DAQ) subsystems based on the computer architectures VME and ATCA. The top-level data control and acquisition is performed with the FireSignal software. The *slow control system* controls the vacuum system, the warning alarm, the gas injection and the energy storage and transport. The *fast control system* is responsible for the power discharge, where the plasma is created and stabilised. Parameters like the plasma's position and the plasma confinement are in the care of this system as well. It's performed by the Multithreaded Application Real-Time executor (MARTe). Every 100 s (real-time cycle), MARTe receives all the new real-time diagnostic data acquired by the control ATCA, processes the data and send the new references to the actuators [3].

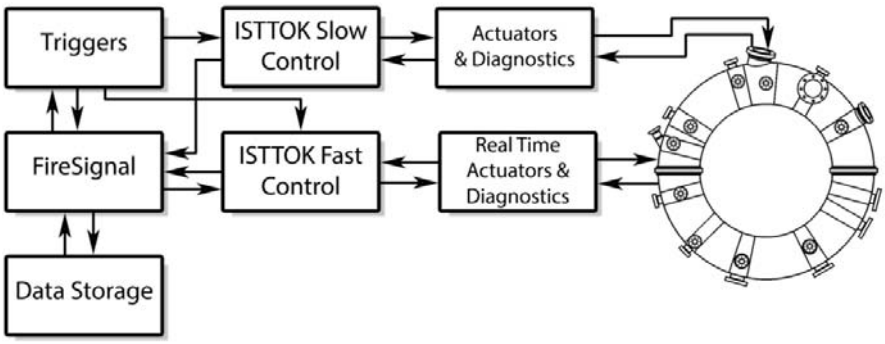

Figure 2.3: *ISTTOK's overall control scheme. The arrows indicate the direction of the information flux, courtesy from Gonçalo Nuno [3].*

2.1.5 *Diagnostic*

ISTTOK diagnostics measure global and local plasma parameter in order to: i) provide information for the real-time control (plasma position, current and density etc.), ii) machine safety (plasma current, density, etc.) and iii) plasma physic. The main ISTTOK diagnostics are presented in Table 2.4 [14]. with indications on the position in tokamak (poloidal and toroidal(ϕ)) and the type of measurement.

The diagnostics position are more clearly represented in Figure 2.4 where HIBD position has been highlighted.

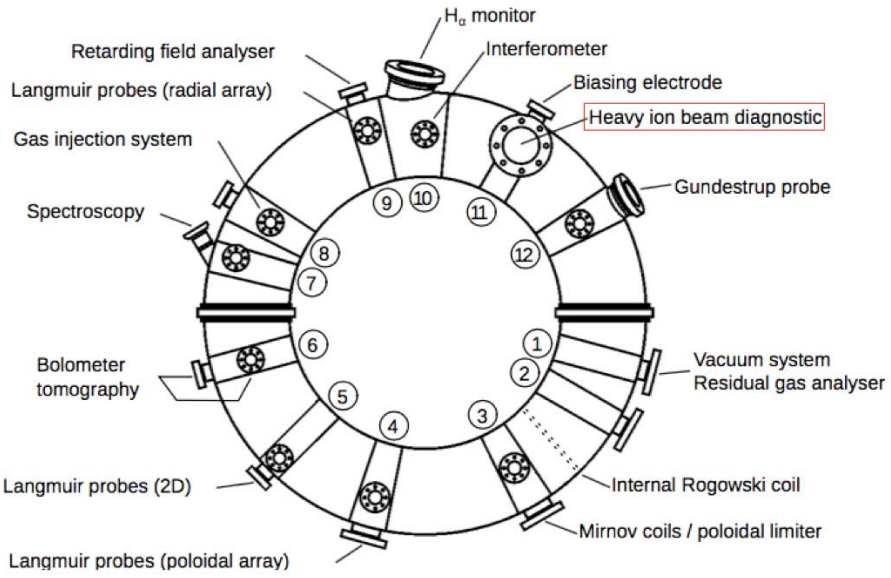

Figure 2.4: *Schematic diagram of ISTTOK ports and diagnostics locations along the torus with HIBD highlighting*

Diagnostic	Measurement	Location
Toroidal loop	loop voltage	\
Internal Rogowski coil	Total I_p	$\phi \approx 45^0$ (full poloidal loop)
Interferometer	line integrated n_e passing through $r = 0$	$\phi = 270^0$ (Top and Bottom)
Hα	Plasma Bulck	$\phi = 270^0$ (LFS)
Langmuir probes (poloidal array)	local at the edge	$\phi = 105^0$ (full poloidal loop)
Langmuir probes (radial array)	radial profile at the SOL and edge	$\phi = 255^0$ (Top)
Langmuir probes (2D)	poloidal and radial profile at the SOL and edge	$\phi = 135^0$(LFS)
Gundestrup probe	local at the SOL and edge	$\phi = 330^0$(LFS)
HIBD	profile at core and core-edge	$\phi = 300^0$ (Top and Bottom)
Spectroscopy	visible and Vacuum Ultra-Violet (VUV)	$\phi = 195^0$ (LFS)
Bolometer tomography	2D plasma reconstruction	$\phi = 165^0$ (Top, LFS and Bottom)
Retard field analyser	profile at the SOL and edge	$\phi = 255^0$ (LFS)

Table 2.4: *Main ISTTOK diagnostics*

2.2 THE HEAVY ION BEAM DIAGNOSTIC

The plasma Heavy Ion Beam Probing method is a unique tool for plasma research in fusion facilities. The HIBP method was realized first at the end of 1960s by Robert L. Hickok and Forrest C. Jobes at a small facility with an arc discharge. Now it has attained the status of one of the most informative diagnostics. [15] After carrying out a D-D measurement, L. Hickok suggested switching over to an H_2^+ beam and looking for an H^+ signal. The H^+ was loud and clear and that was the last of the nuclear measurements. One of the first things done using the molecular break-up of the H_2^+ was to measure the density of the hollow cathode arc plasma was a study of a coherent instability. In 1970 and for the first time invented by F. C. Jobes and R. L. Hickok, was designed and used to measure directly the plasma space potential. [16] At ISTTOK, a new concept of the HIBP was developed in the early 90's by using a multiple cells array detector (MCAD). With this new technique, it was possible to diagnose the whole plasma column: all the sample volumes are measured simultaneously instead of probing single sample volumes successively. Furthermore, the HIBP at ISTTOK has the unique particularity of also collecting the primary ion beam current, which can then be used for the absolute density profile reconstruction. For these reasons and to distinguish the two concepts, the term "probe" (P) in HIBP was changed to "diagnostic" (D), resulting in HIBD. [4]. In the present ISTTOK HIBD configuration three local plasma parameters can be retrieved: i) plasma density (n_e), ii) electron temperature (T_e), iii) poloidal magnetic field (B_p) and iv) plasma potential (V_p).

2.2.1 *Basic Principles*

The HIBD operation consists of an ions beam injections I^+ in ISTTOK HIBD) inside the plasma in a parallel direction with respect to the toroidal magnetic field. The present HIBD in ISTTOK tokamak uses Xe^+ (or Cs^+) as ion species with energy between 20– 25 keV. The primary beam I^+ is ionized along the path for the interaction with the plasma generating a secondary beam I^{2^+}. The secondary beam is so separated from the primary beam under the action of the toroidal magnetic field (Lorentz force) that deflections in a semi-circular trajectory. The Larmor radius of the secondary beam trajectory is half of the radius of the primary beam because of the different charge of the two beams (I^{2^+} and I^+). The primary and secondary beam are so detected by the 2D Multiple Cell Array Detectors (MCADs) outside the chamber as showed in Figure 2.5 and the plasma parameters are determinate measuring of the beams intensity, position and energy. [17]

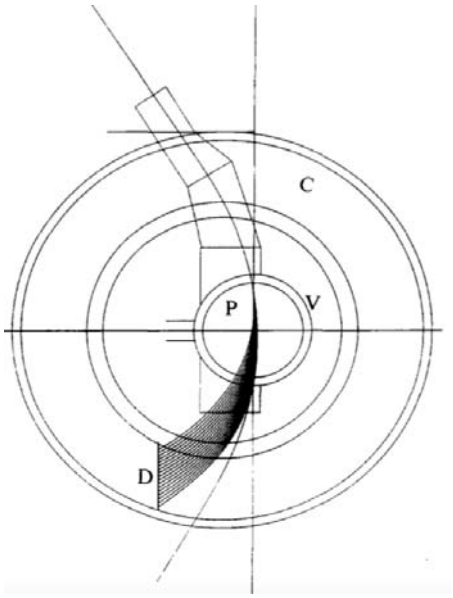

Figure 2.5: *The HIBD set-up and ion beam trajectories: (V) vacuum vessel wall; (P) plasma*, courtesy from J. A.C. Cabral [4]

2.2.2 *Hardware components*

The main HIBD hardware components are the i) Injector system, ii) Electrostatic Input Module (EIM), iii) Cylindrical Electrostatic Analyzer (CEA) and the vi) MCADs.

Injector system

The injector generates the heavy-ion beam and injects it into the plasma. It is composed of:

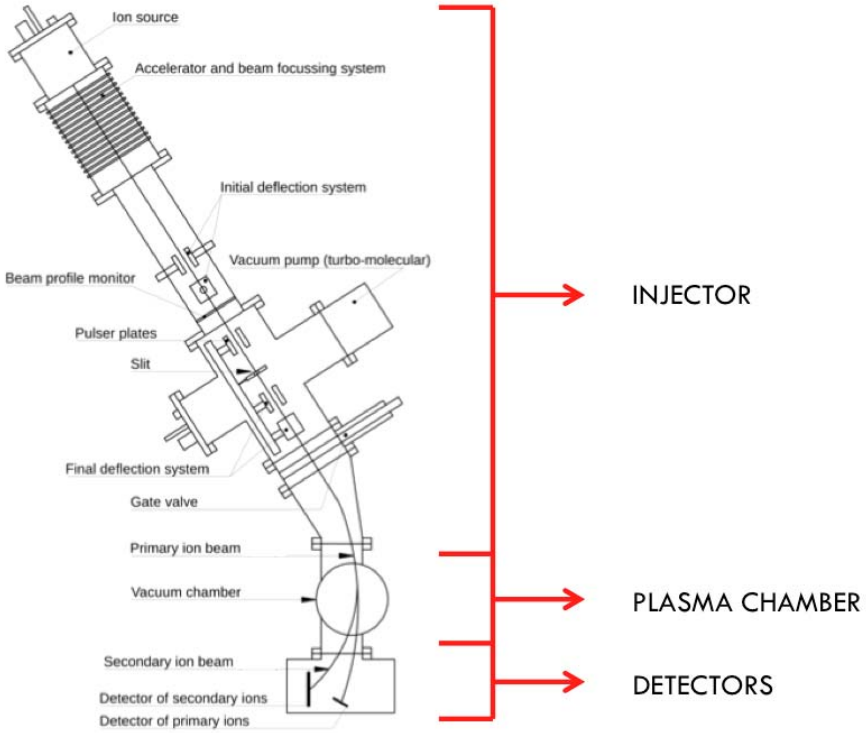

Figure 2.6: *Schematic representation of the HIBD Injector system*

- The *Ion source* is responsible for generate a plasma by ionizing the surrounding gas (Xe) by means of thermo-electrons emitted by a Tungsten filament that is biased with respect to the chamber wall in order to accelerate the electrons generating an arc .

- The *Extraction, acceleration and beam focussing system* is composed by a quasi-Pierce electrode that extract the positive ions from the plasma inside the ion source chamber and by a multi-electrode acceleration tube split in two parts. The first part accelerates the beam (gap up to 25kV) while the second part focus the beam with an optic configuration.

- The *Deflection system* deflects toroidally and radially the beam, it is divided in two parts. The initial deflector aligns the beam to the pin hole while the final deflector aligns the beam trajectory to the Front Multiple Cell Array Detector.

- The *Beam profile monitor*: is used to measure the spatial distribution of the beam current. The monitor consists of a pair of conducting wires constituted by two parallel wires.

- The *Pulser and slit pin-hole*: consists of two parallel conducting plates and of a a circular hole with 3 mm of diameter The Pulser is used to modulate the beam chopping it at a desired frequency while the pinhole defines the beam diameter.

EIM and CEA

Measurements of the plasma potential in ISTTOK have been realized in the past by the time of flight (ToF) technique [14]. This method requires relatively long integration in time (for meaningful statistics) therefore not suitable to follow local plasma potential fluctuations. In order to measure the plasma potential fluctuations at several points a new 90^0 cylindrical electrostatic energy analyzer (CEA) is being designed and developed. In order to implement the CEA system to the Injector and detector systems and adapt it to the spatial disposition of the ISTTOK components an Electrostatic Input Module (EIM) has been installed. Thus the Plasma potential measurement system can be divided into two interconnected main stages (as depicted in Figure 2.7), the electrostatic input module (EIM) which collects and shapes the secondary beams and the cylindrical electrostatic energy analyzer (CEA) [5].

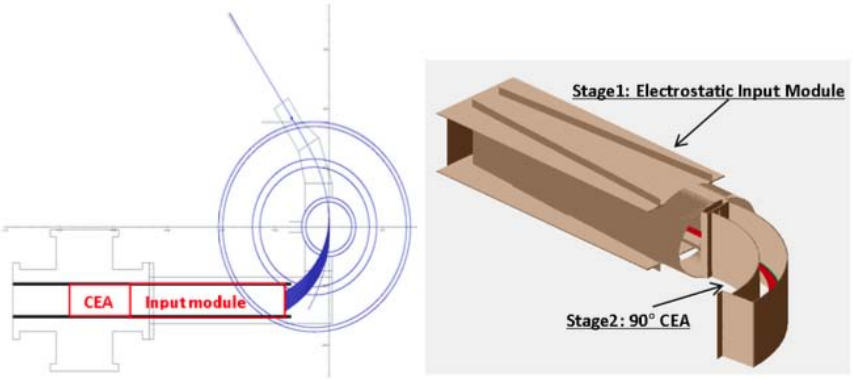

Figure 2.7: *The setup presenting the HIBD in ISTTOK with the arrangement of the electrostatic input module (EIM) and CEA (on the left) and the 3D arrangement of the main stages, courtesy from R. Sharma [5]*

The **Electrostatic Input Module** collects, deflects and focus four beams emerging from four different plasma radius fig. 2.8 (the EIM input slit defines the beam vertical dimension of 8 mm and the slit separation determines the plasma sample volume radial separation of about 15 mm). The main EIM components are:

- 30^0 *electrostatic cylindrical plates plus four pairs of parallel plates*: The purpose of this arrangement is to direct and center the beams into the multiple aperture Einzel-like electrostatic lens.
- *Multiple aperture Einzel-like lens* consists of four planar vertical electrodes with four apertures which provides the required electric field gradient for shaping the four passing beams. The side strip electrodes allow for beam shaping and deflection in the horizontal direction. [5].

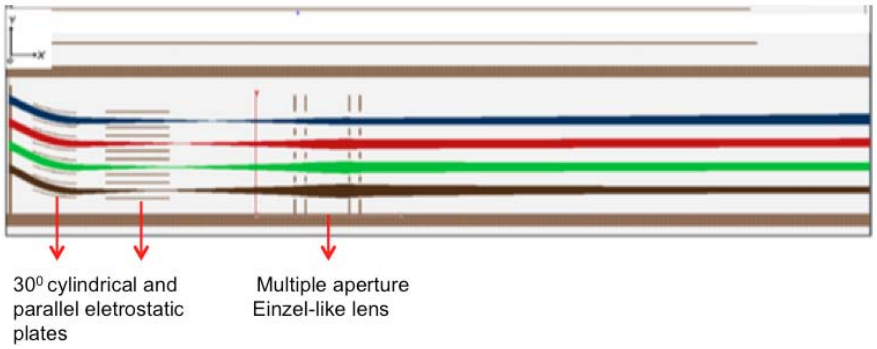

Figure 2.8: *2D representation secondary beam channels passing through EIM, courtesy from R. Sharma [5]*

The **90⁰ Cylindrical Electrostatic Energy Analyzer** 2.9 provides three functions: i) beam energy retardation, ii) beam focusing and iii) energy analysis. It consists of a combination of transversal input/output parallel plate arrangement embedded in the longitudinal cylindrical plate geometry. The resulting field lines present a retardation stage with positive lensing followed by the analyzer stage exhibiting co-cylindrical potential lines. The CEA geometrical parameters are showed in Table

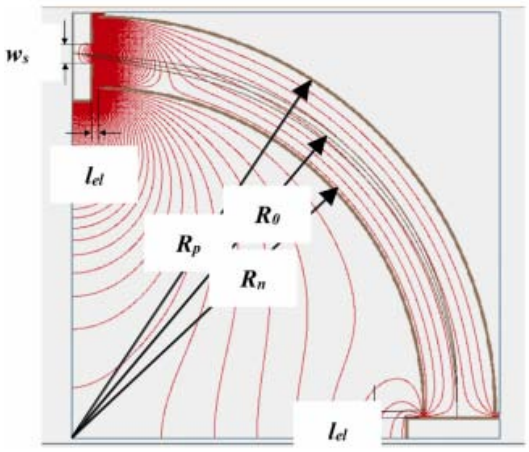

Figure 2.9: 90^0 *cylindrical energy analyzer considered for SIMION simulations. The resulted equipotential lines are also shown, courtesy from I. S. Nedzelskiy [6]*

2.5 The CEA optimal operation conditions are showed in Table 2.6

R_p	R_n	R_0	l_{el}	w_s
275	225	250	2	5

Table 2.5: *Geometrical Parameter [mm]*

V_p	V_n	PSI
8.406	7.6	8.03

Table 2.6: *Optimal operation conditions*

Detectors

The Multiple Cell Array Detectors (MCADs) are flat matrixes of copper cells. The MCADs used to develop this thesis project (Figure 2.10) are:
Front MCAD is located at the entrance of the EIM, it is composed of 11 rows (height = 8 mm), four of them are split toroidally in three columns. The four slits ($8 \times 4mm^2$) on the front detector that defines the selection of four secondary beams to be passed into the EIM. With this detector it is possible to obtain the toroidal position of the secondary ions (used for the poloidal magnetic field measurements) and also the $n\sigma(T)$ quantity. Each detector row corresponds to a unique radial position of the plasma sample volume so that the cell size of the Detector define the measurement resolution.
Intermediate MCAD is located at the entrance of the CEA and is composed of four side cells ($31 \times 7mm^2$) that surround the long slit ($62 \times 5mm^2$), these cells are not active during the thesis project experiments.
Back MCAD is located at the end of the CEA and is used in a configuration of two cells ($210 \times 150mm^2$), With this detector it is possible to obtain the plasma potential from the displacement of the standard CEA trajectory .

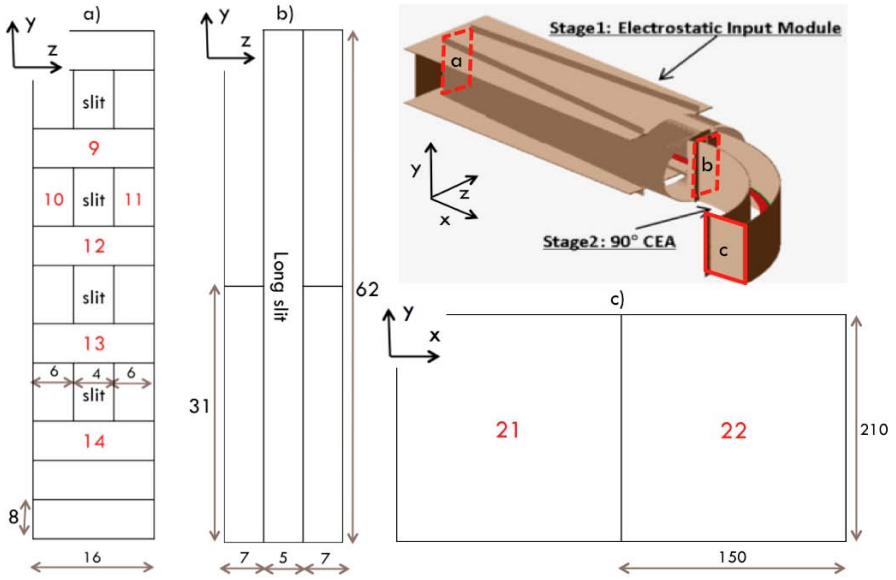

Figure 2.10: *Schematic representation (not to scale) of the Front detector a) Back detector b) and Intermediate detector c) with its respective active cells dimension value [mm], reference channels number (red) to get data from SDAS server and MCAD position in the CEA and EIM stages*

2.2.3 *Local Measurements*

The HIBD provides local measurements from several sample volumes located along the primary beam path in the plasma volume. There is a bi-univocal correspondence between the plasma sample volume analyzed coordinate and the detection cell position. The determination of the n_e and T_e radial profiles is based on the retrieval of the generation factor $n_e(r_j)\sigma_{12}T_e$ along the primary beam path from the ion currents collected by the MCADs while the determination of the B_p and V_p profile is based on the retrieval of the Toroidal Shift respectively on Front and Back MCADs.

Plasma Density and Electron Temperature

The current of a secondary beam created at the sample volume radial location r_j is given by:

$$I_j^{2^+} = 2n_e(r_j)\sigma_{12}(T_e(r_j))I_j^+ dl \tag{2.1}$$

The Generation factor $n_e(r_j)\sigma_{12}$ can not be computed implementing the secondary and primary detected beam current ($I_{j(det)}^{2^+}$, $I_{j(det)}^{+}$) to the equation 2.1 because of the attenuation factor due to the double ionization of the primary beam $(n_e\sigma_{13})$ and the attenuation factor due to the ionization of the secondary beam $(n_e\sigma_{23})$. The Generation factor can so be estimated by equation ;

$$I_{j(det)}^{2^+} = 2ABn_e(r_j)\sigma_{12}I_0^+ dl \tag{2.2}$$

Where A ,B are the primary and secondary beam attenuations, respectively and I_0^+ is the initial beam current. [17].

Electron Temperature T_e measurements may be performed by injecting into the plasma two beams of different species following the same trajectory. From the collected currents the $n_e\sigma_{qm}$ factor of each species can be determined and T_e retrieved from their ratio:

$$\Re_e = \frac{\left[n_e\sigma_{qm}\right]_{M_1}}{\left[n_e\sigma_{qm}\right]_{M_2}} = \frac{\left[\sigma_{qm}(T_e)\right]_{M_1}}{\left[\sigma_{qm}(T_e)\right]_{M_2}} \tag{2.3}$$

which is a known function of electron temperature through the ratio of the individual effective cross sections. In Equation 2.3 q and m represent the charge state of the ion, respectively, before and after the ionization.

Electron Density n_e profile is determined by dividing $n_e\sigma_{qm}(T_e)$ of any species by its $\sigma_{qm}(T_e)$ for the formerly measured T_e values. [17]

Poloidal Magnetic Field

The local poloidal magnetic field radial profile, generated by the plasma current, can be estimated by i) the toroidal (z) detected shift on Front MCAD due to the $v_b \times B_p$ cross product (Lorentz force) and ii) the primary and secondary beam time of flight of the (T_1 and T_2) T_1 and T_2 can be estimated by a numerical code that simulates the ion trajectory and uses it to compute the avarage z-velocity v_{z-j} of each ion beam [4]

Figure 2.11: *Front MCAD and toroidal shift (z) direction schematic representation*

As the beam trajectories are approximately perpendicular to the poloidal magnetic field lines two consecutive double ionized ions (r_j and $r_{(j+1)}$ radial location) follow the same trajectory interacting with the same Magnetic field except for the d_s distance from r_j to r_{j+1}. Along 'd_s path the j-ion is doubled charged with respect to the (j+1)-ion determining an increase of the z-velocity dv_z :

$$dv_z = v_j - v_{(j+1)} \tag{2.4}$$

The two ions will then follow their trajectories keeping the same velocity difference dv_z , thus increasing their spatial separation with time. Poloidal Magnetic field B_p is related to the z-velocity increase dv_z by the following equation:

$$dv_z = \frac{e}{M} B_p v_r \frac{ds}{v_b} \tag{2.5}$$

where M is the heavy ion mass, v_r is the radial component of the beam velocity and $\frac{ds}{v_b}$ is the time the primary beam takes from one ionization point to the next one.

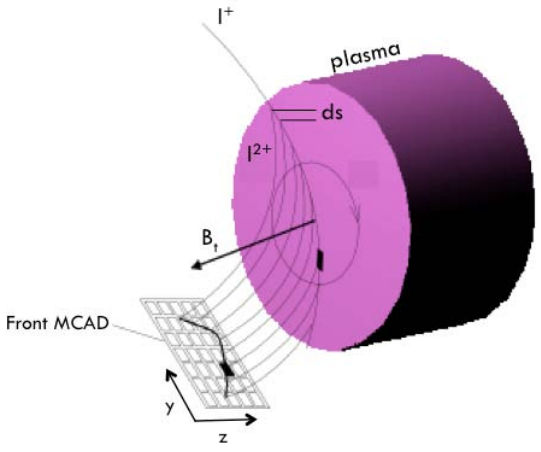

Figure 2.12: *Schematic primary and secondary beam trajectory representation*

By the numerical code we can compute the time of flight of all secondary ions, from r_j to the detector. So, the time derivative of the final z-coordinate, divided by the secondary time of flight, T_2, will be a measure of the z-acceleration and therefore of the poloidal field component orthogonal to the ion trajectory. As explain in [4] in order to overcame the neglected effect of the e.m. field gradients on the two adjacent trajectories a complementary algorithm has been developed to retrieve the poloidal field profile from the knowledge of only the detector characteristics $z = z(y)$ and the times of flight of the primary as well as the secondary ions, T_1 and T_2.

Plasma Potential

The basic principle behind the measurement of the plasma electrostatic potential is energy conservation. The beam starts with an initial energy E_i given by the acceleration voltage. Then, is assumed that i) the beam exits the accelerator at ground potential before entering the plasma, ii) the detector is at ground potential, iii) the kinetic energy of the ions does not change due to the ionization process, i.e., the kinetic energy variation due to the loss of one or more electrons is negligible. As the particles pass through the plasma, the total energy which is the sum of the kinetic and potential energy of $-e\phi_{SV}$ are stripped off where e is the electron charge and ϕ_{SV} is the electrostatic potential at the sample volume. The total energy of the secondary ion is therefore $E_i + (q_s - q_p)\phi_{SV}$ where q_p is the primary ion charge. This energy is conserved as the ion passes out of the plasma to the detector. Therefore the plasma potential localized to the sample volume position can be obtain from [**?**]:

$$\phi_{SV} = \frac{E_d - E_i}{q_s - q_p} \tag{2.6}$$

where E_d is the beam energy at the detector. In order to measure this energy beam variation a 90^0 Cylindrical Electrostatic Analyzer has been implemented . For the conventional cylindrical analyzer the ion displacement r from the standard trajectory at the analyzer end detector plate is given by (first order estimation) [5] :

$$\Delta r = \delta r + C_\theta \delta\theta + C_E \delta E \tag{2.7}$$

Where, $\Delta r = \frac{R}{R_0}$, is the normalized initial position of the ion relative to standard trajectory (of radius R_0) and $r = \frac{\Delta r}{R_0}$ is the analyzer normalized input slit location, C_θ is the first-order angular aberration coefficient, $\delta\theta$ is the angle of beam trajectory relative to the standard trajectory, C_E is the energy dispersion coefficient and $E = \frac{E}{E_0}$ is the normalized ion energy. The Beam Energy variation is so correlated to the beam Toroidal Shift (x) on the Back Detector (fig. 2.13).

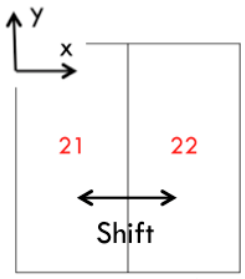

Figure 2.13: *Back MCAD and toroidal shift (x) direction schematic representation*

3

CHARACTERISATION OF THE CEA MEASUREMENTS

The aims of the thesis project are to i) develop a data analysis program in Matlab environment that acquire and process data produced by the Heavy Ion Beam Diagnostic (HIBD), in order to ii) demonstrate the expected low correlation between the Beam Toroidal Shift on Front MCAD and the Beam Toroidal Shift on Back MCAD and to iii) compute an approximate value of the secondary beam passing through the slit. The first section of this Chapter presents how the heavy ion beam signals are processed before any data analysis is performed. The second and third sections describe the Data Analysis routine and presents a qualitative interpretation of the results obtained.

3.1 DATA PROCESSING

The developed Matlab program automatically processes the acquired HIBD Signals in order to perform the data analysis with manageable signals. The data processing section will describe the process routine referring to two shots: 47605 and 47604.The main automatic functions are:

- Acquire and filter multiple Signals
- Synchronization of chopping Signal with Detected Signals
- Noise removing
- Signals cross-correlation
- Signals interpolation on Front Detector

3.1.1 *Data Acquisition and Selection*

The ISTTOK diagnostic data is acquired from the Shared Data Access System (SDAS) server that allows access to the ISTTOK database. This server provides an interface layer between the end-user and the database allowing a database management system (DBMS) independent/abstraction. Each set of data is identified by :

- Unique identifier code (example: ' *PCIE_ATCA_ADC*_16.*BOARD*_3.*CHANNEL*_009) that distinguish between different type of data (Plasma current, the detected Signal at ch.9 ecc.)
- Event code (example : 47605) that identifies the analyzed HIBD shot number

The HIBD Signal sample frequency is 2000 KHz in an acquisition time period up to 600 ms that corresponds to $\sim$ 1200000 sample points. The Plasma Current and Pulser Signal are also acquired in order to implement the processing functions of the HIBD Signals. The Cylindrical plates have been biased in order to analyse the secondary beam signal $I^{2+}_{j(det)}$ that passes through the second slit (Figure 3.1) of the Front MCAD on the time range of the positive cycles ($\sim$ 4000 A)

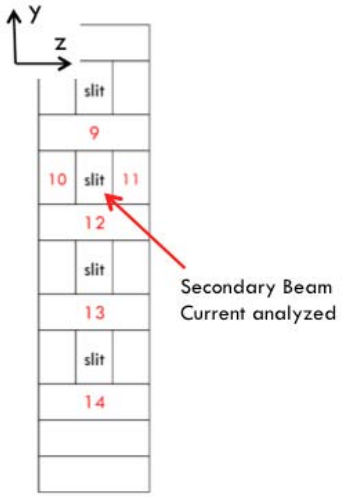

Figure 3.1: *Schematic Front MCAD and secondary beam current direction* $I^{2+}_{j(det)}$ *representation*

The HIBD has been biased to analyze the signal on positive plasma currents so the Signals data are automatically selected, divided and stored by the program in a set of data (Cycles) imposing a level condition referred to the plasma current positive cycles as shown in fig. 3.2

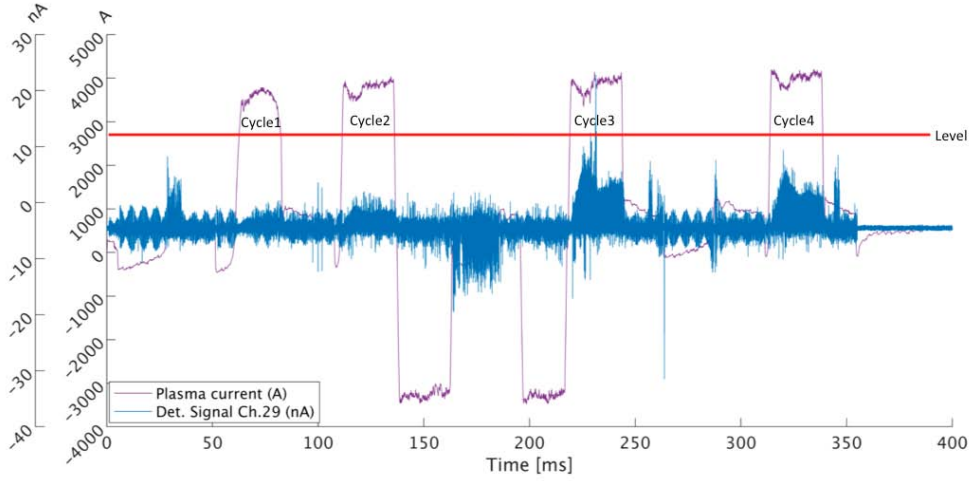

Figure 3.2: *Plot of Plasma Current and HIBD Signal on Back detector ch.29,* $f_{chop} = 20$ *KHz,* $f_{low-pass} = 200$ *KHz, Time* $[0\ 400]$ *ms, Shot47605*

3.1.2 *Cross-Correlation*

In signal processing, cross-correlation is a measure of similarity of two series as a function of the temporal displacement of one relative to the other. The cross-correlation is based to the covariance concept: if x and y are two discrete signals of n sample points, $\bar{x}$, $\bar{y}$ and σ_x, σy are the respective mean values and standard deviations, the normalized covariance between x and y is expressed by the Equation 3.1 :

$$r = \frac{\frac{1}{n}\sum_{i=1}^{n}(x_i - \bar{x})(y_i - \bar{y})}{\sigma_x \sigma_y} \tag{3.1}$$

The covariance is usually normalised as showen in 3.1 in order to remove the dependence on the absolute value. The coefficient r describe the x and y linear dependence and has values in the range of $[-1 + 1]$, $r = 1$ mean full correlation, $r = 0$ mean absence of correlation while $r = -1$ mean negative correlation. In the diagnostic application, the covariance may not be the most adequate signal comparison method because of the possible presence of time lags not take into account between signals that are carrying or not the same information obtained by two devices placed in different locations, so that the cross-correlation is used. The cross correlation r_{xy} give the covariance information in function of the sample lags m and it is expressed by the Equation 3.2 :

$$r_{xy} = \begin{cases} \frac{\frac{1}{n}\sum_{i=0}^{n-m-1}(x_{i+m} - \bar{x})(y_i - \bar{y})}{\sigma_x \sigma_y} & if\ m \geq 0 \\ \\ r_{yx}(-m) & if\ m < 0 \end{cases} \tag{3.2}$$

To have an estimate of the cross-covariation (formally equivalent to a non-normalized cross-correlation) the Matlab function *xcov* was used, that computes:

$$c_{xy} = \begin{cases} \sum_{i=0}^{i-m-1}(x_{i+m} - \frac{1}{n}\sum_{i=0}^{n-1} x_i)(y_n - \frac{1}{n}\sum_{i=0}^{n-1} y_i) & if\ m \geq 0 \\ \\ c_{yx}(-m) & if\ m < 0 \end{cases} \tag{3.3}$$

The result is then divided by the mean values and standard deviations σ_x, σ_y computed by the matlab function *std* in order to obtain the equivalent normalized cross-correlation r_{yx}. This function was implemented in the data analysis program for two main operations: i) synchronization of the Pulser Signal with the HIBD Signal (see section 3.1.3) and ii) shift signals analysis (see section 3.3)

3.1.3 *Synchronization*

The Pulser signal shows an off-set of a small number of samples with respect to the HIBD signal as showed in fig. 3.3. The synchronization between the two signals is a condition for the noise removing function has explained in section 3.1.4 so that the HIBD Signal is automatically synchronized computing the cross-covariation between the Pulser Signal and the HIBD Signal of the whole signal for few sample shift m, with m variation in the range of $[-20 \ +20]$. The sample shift m_{max} location of the cross-covariance maximum absolute value r_{max} has to correspond to the sample shift of de-synchronization. Thus once retrieved m_{max} from the cross-covariance function output is possible to correct the mutual Signals time position in the interval Δt as shown in fig. 3.3

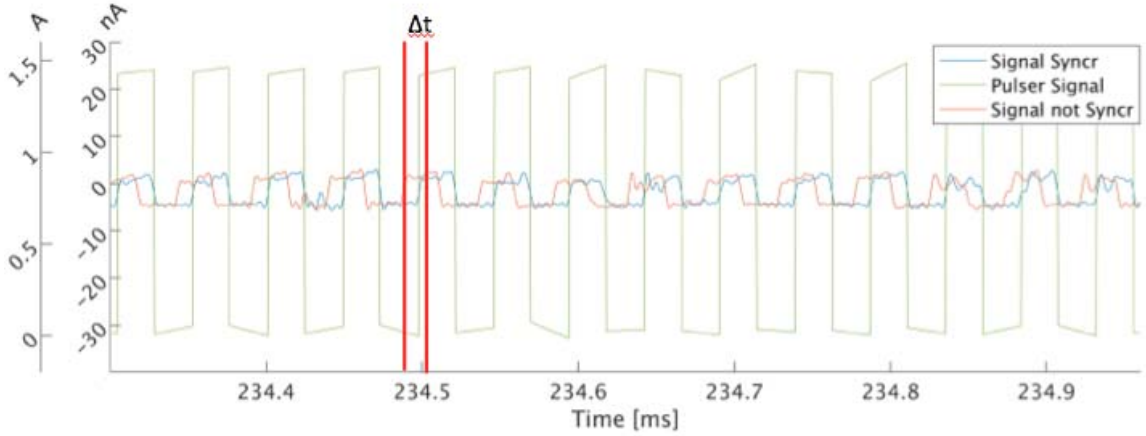

Figure 3.3: *Plot of HIBD Signal on Back MCAD ch.29 before and after synchronization,* $f_{chop} = 20KHz$, $f_{low-pass} = 200$ *KHz, Time* $[235.3 \ 235.8]$ *ms, Shot* 47605

3.1.4 *Noise Removing*

The HIBD signals are usually modulated by a square wave (chopped beam: beam ON and beam OFF) generated by the pulser in order to discriminate the beam from the background noise level and characterise the background in terms of fluctuations. For this thesis project the HIBD Signals have been modulated with a chopping frequency of $f_{chop} = 20$ KHz. In Figure 3.4 is showed a typical HIBD signal from a secondary beam detector cell and the references of the Pulser Signal and Plasma Current Signal.

The signal from a detector cell j – $I_{j(det)}$, is composed of: the heavy ion beam current - $I_{j(PRI)}$, the current due to the secondary emission electrons - $I_{j(SE)}$, the current from the photo-electric effect due to the plasma ultra-violet radiation - $I_{j(UV)}$ and the noise from the acquisition

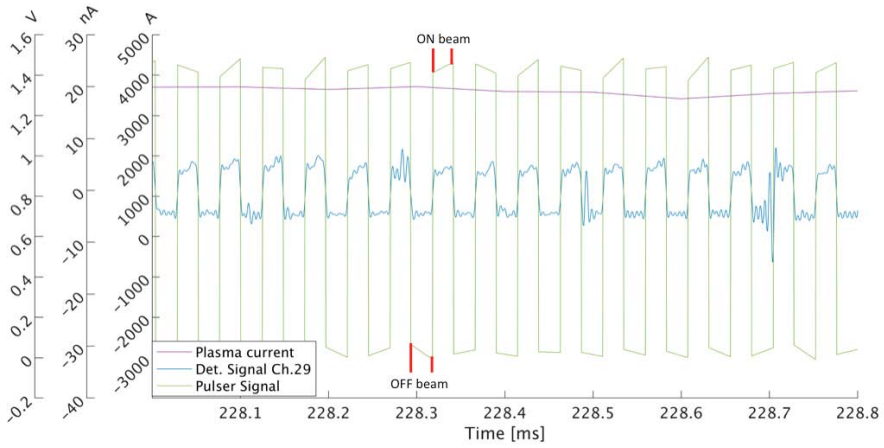

Figure 3.4: *Plot of Plasma Current, Pulser Signal and HIBD Signal on Back MCAD ch.29 , f_{chop} = 20 KHz, $f_{low-pass}$ = 200 KHz, Time* [228 228.8] *ms, Shot47605*

system - $I_{j(ACQ)}$ The equation system describes the dependence of these $I_{j(det)}$ components to the ON and OFF time range:

$$\begin{cases} \mathrm{I}_{j(det)} = I_{j(PRI)} + I_{j(UV)} + I_{j(SE)} + I_{j(ACQ)} & \text{if beam is ON} \\ \mathrm{I}_{j(det)} = I_{j(ACQ)} + I_{j(UV)} & \text{if beam is OFF} \end{cases}$$

The noise removing routine reduces the components of the current due to the plasma ultra-violet radiation - $I_{j(UV)}$ applying the fast chopping technique and the current from the acquisition system - $I_{j(ACQ)}$ applying a low pass filter as described in the next sections.

Low-pass Filter

The Power Spectrum of the HIBD Signals highlights that the current from the acquisition system $I_{j(ACQ)}$ is relevant for frequency higher than 200 KHz and observable for all the HIBD Signals, an example is showed in fig. 3.5

In order to remove the $I_{j(ACQ)}$ component before the selection routine a FIT digital low-pass filter is applied using an *dsp.LowpassFilter* Matlab object characterized by Filter Order N of 3000 and a PassbandFrequency $f_{low-pass}$ of 200 KHz, an example of reduction effect is showed in fig. 3.6

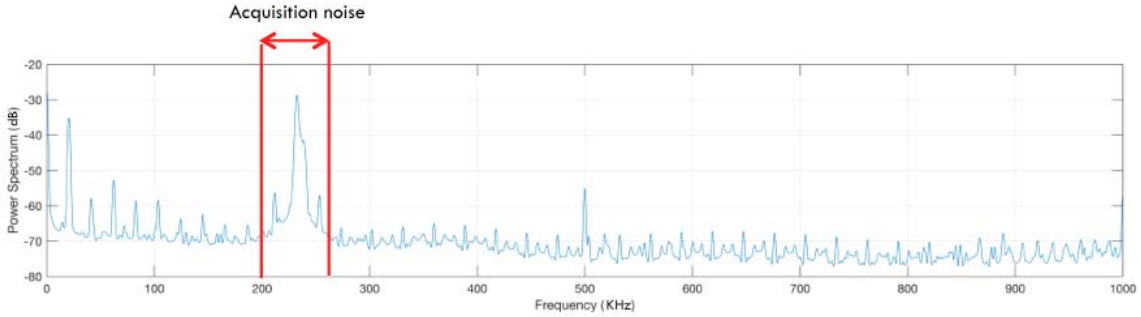

Figure 3.5: *Shot* 47605 *and the corresponding Power Spectrum with noise frequency range reference*

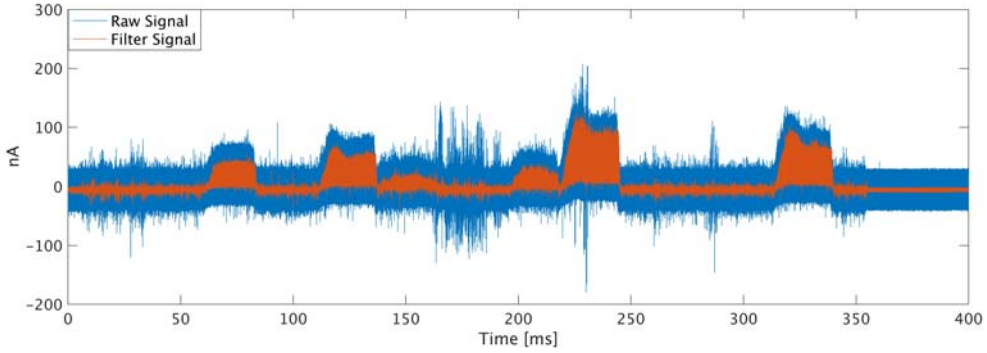

Figure 3.6: *Plot of HIBD Signal on Front detector ch.*9, $f_{chopping} = 20$ *KHz*, $f_{low-pass} = 200$ *KHz*, *Time* $[0\ 400]$ *ms*

Fast chopping technique

The Fast chopping technique consists in modulating the HIBD signals at medium to high frequency (10 KHz $< f_{chopping} <$ 200 kHz) in order to consider the background noise $I_{j(ACQ)}$ during the beam OFF and ON periods in the condition of interest: $f_{chopping} > 2 \times f_{(UV)}$ and $f_{(PRI)}$ that are respectively the fluctuation frequency of the plasma ultra-violet radiation and of the primary current.
The method used to remove the background noise consists of the following steps:

1. ON and OFF beam points detection
2. Compute the mean of the beam OFF and ON sample points as showed by the example in fig. 3.7 where the sample points used for the calculation of the ON and OFF means have been highlighted. During the beam OFF and ON periods, it is assumed that both plasma and background are frozen, i.e., the chopping frequency is "much higher" than any frequency contained in plasma or background signals. In this way, the higher the chopping frequency the more the plasma and background fluctuations can be assumed as frozen. On the other hand, the lower the number of available sample points for performing the mean (because of higher chopping frequency) the higher the statistical error on the mean calculation.

3. Interpolate background noise means with a linear interpolation

4. Subtract the ON mean values to the OFF interpolated values at the corresponding time instant, the result is an under-sampled Signal.

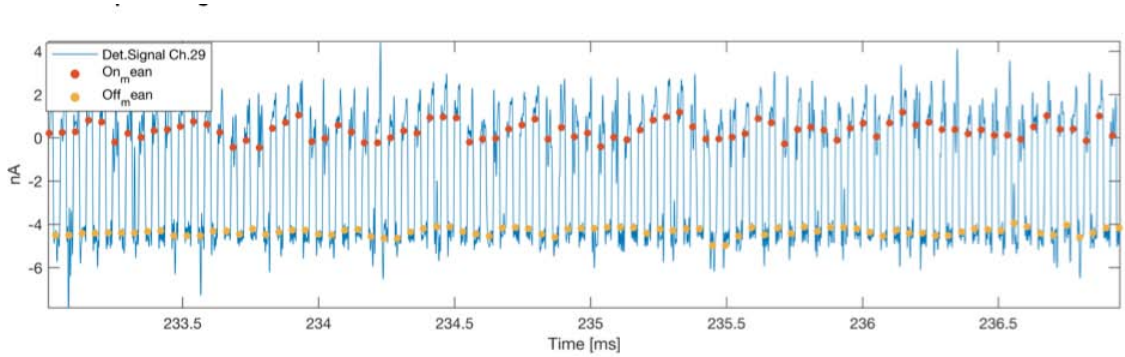

Figure 3.7: *Plot of the HIBD Signal on Back detector ch.29 with ON and OFF beam means representation,* $f_{chopping} = 20$ *KHz,* $f_{low-pass} = 200$ *KHz, Time* [233 237] *ms, Shot47605*

In order to detect the ON and OFF beam points the program localizes a set of reference points as shown in fig. 3.8 on the Pulser Signal imposing a double condition : i) the points must be below the mean of the Pulser Signal and ii) the points must be closed to a slop change of a prescribed amplitude, for this purpose the difference quotient was performed for each couple of subsequent sample points $I_{j(det)}$ and $I_{j+1(det)}$, when the condition $\frac{I_{j+1(det)} - I_{j(det)}}{\Delta t} > 200$ (positive slope) or $\frac{I_{j+1(det)} - I_{j(det)}}{\Delta t} < -200$ (negative slope) are met the sample point $I_{j(det)}$ is stored in a separate vector.

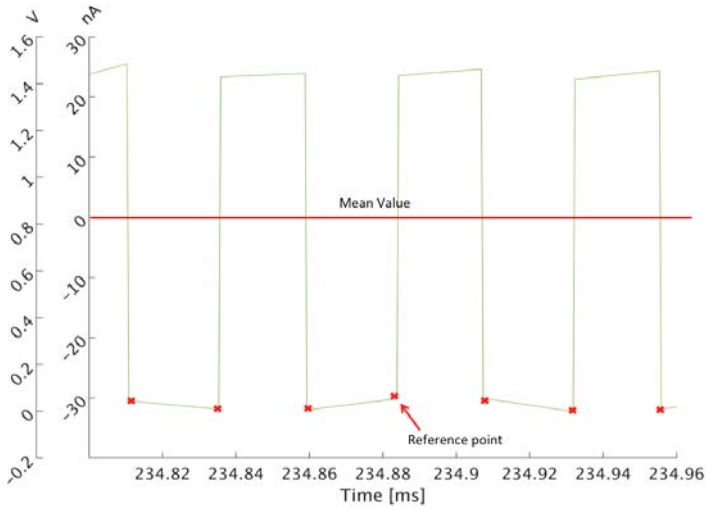

Figure 3.8: *Plot of HIBD Signal ch.29, Pulser Signal and the set of reference points,Shot* 47605

For signal-ON reconstruction and averaging, for every subsequent couple of the reference points the corresponding beam-ON (and beam-OFF) beam points time interval range location is retrieved, as shown in fig. 3.9 , by decreasing 20% the time interval of L between each couple in order to exclude the transition points (20% value have been empirically determinated).

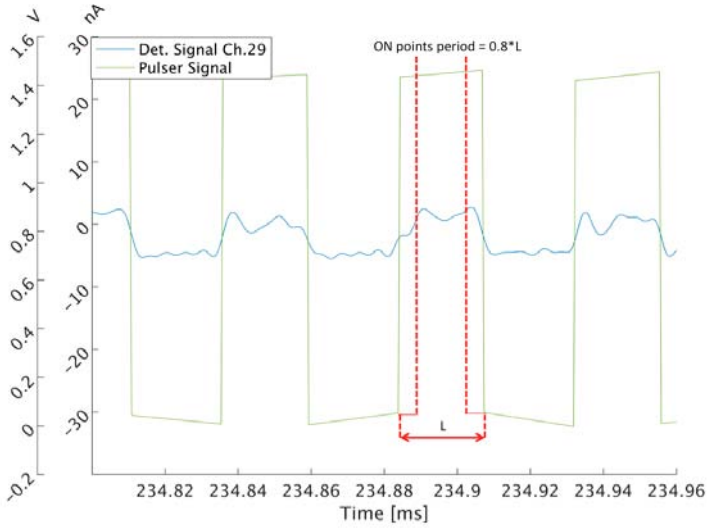

Figure 3.9: *Plot of HIBD Signal ch.29, Pulser Signal and the set of reference points, Shot* 47605

The HIBD Signals are influenced by different spikes caused by the Electromagnetic External Interferences that may affect the correct computing of the ON and OFF beam mean values. The program uses a dedicated routine in order to localize the spikes and correct the corresponding mean value, an example is showed in fig. 3.10

The spikes are detected applying two different conditions depending on the direction and localization of the spike, an example is showed in fig. 3.11. The conditions are i) h_1 and $d_2 > a \cdot A$ and ii) d_1 and $d_2 > b \cdot A$, where:

- a, b : values empirically determinate, $a = 0.018$ and $b = 0.015$
- A : amplification factor nA/V , $A = 100$ on the Front Detector and $A = 500$ on the Back detector
- h_1 : distance between the Maximum (ON) or Minimum (OFF) Values of the j and $(j-1)$ time periods respectively ON or OFF
- h_2 : distance between the Maximum (ON) or Minimum (OFF) Values of the j and $(j+1)$ time periods respectively ON or OFF
- $d1$: distance between the local Minimum (ON) or Maximum (OFF) Values of the j and $(j-1)$ time periods respectively ON or OFF
- $d2$: distance between the local Minimum (ON) or Maximum (OFF) Values of the j and $(j+1)$ time periods respectively ON or OFF

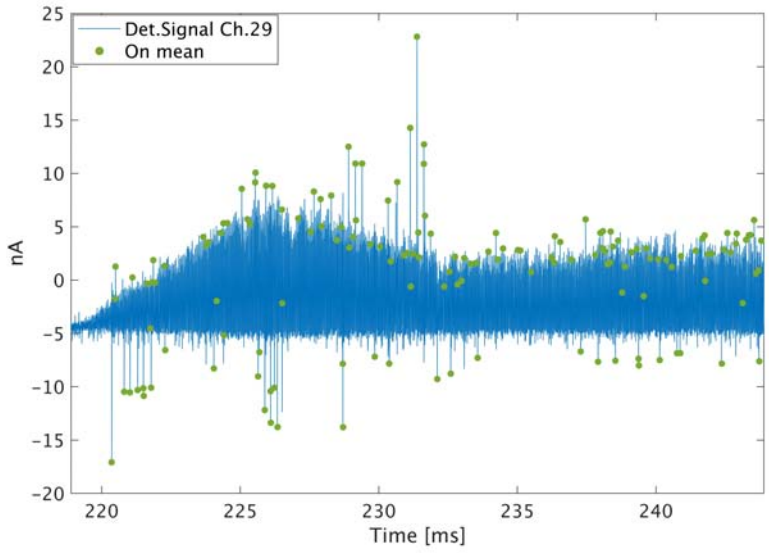

Figure 3.10: *Plot of Plasma current and HIBD Signal ch.29 with spikes reference points representation,* $f_{chopping} = 20$ *KHz,* $f_{low-pass} = 200$ *KHz, Time* $[220\ 245]$ *ms, Shot47605*

For each detection localized at the j_{ON} or j_{OFF} time periods , the corresponding j mean is equalized to the $(j-1)$ mean value of the previous ON or OFF time period $j_{mean} = (j-1)_{mean}$

The last step of the Fast Chopping method is to interpolate the OFF mean points and subtract the ON mean values to the OFF interpolated values at the corresponding time instant. As the background noise I_{UV} is present both on ON and OFF beam the previous procedure remove the noise component from the ON means giving as result an undersampled clean signal as shown in fig. 3.12, where the sample points are highlighted in red.

3.2 APPROXIMATE SLIT CURRENT VALUE

The second task of the thesis project is to compute an approximate value I_{interp} of the current passing through the second slit (counting from the top) of the Front MCAD, the location is shown in fig. 3.13

The information about the secondary current beam intensity $I_{j_{2+(det)}}$ that is correlated to the $n_e\sigma(T)$ measurement and pass through the slit is missed. Because this part of the beam current is partially captured inside the EIM-CEA chain its value may be recovered. One alternative way to recover the value of this current is by 2D interpolation of the front detector cells.
Computing a suitable approximation is based upon:

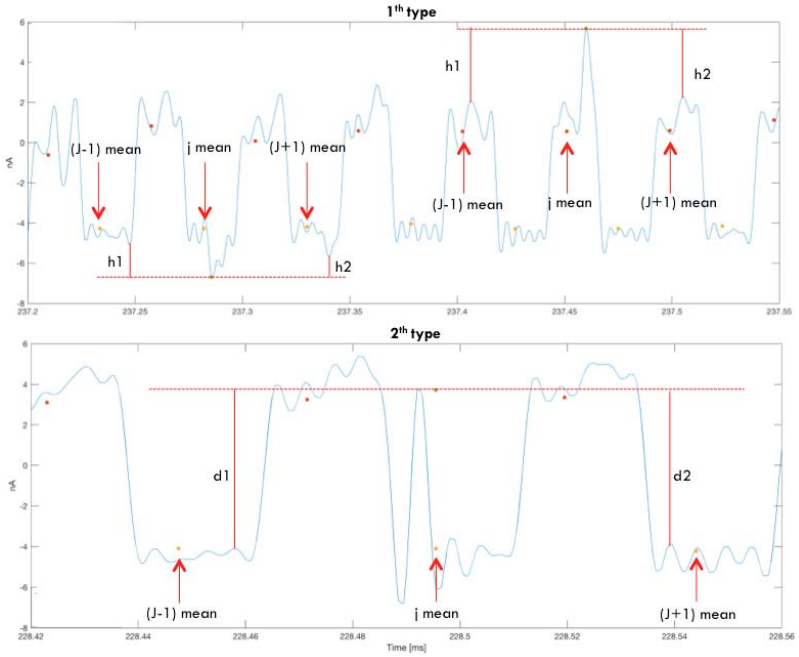

Figure 3.11: *Plot of Plasma current and HIBD Signal ch.29 at* [237.22 237.55] *ms (Higher Picture) and* [228.42 228.56] *ms (lower Picture) with spikes detection method representation,* $f_{chopping} = 20$ *KHz,* $f_{low-pass} =$ 200 *KHz, Shot* 47605

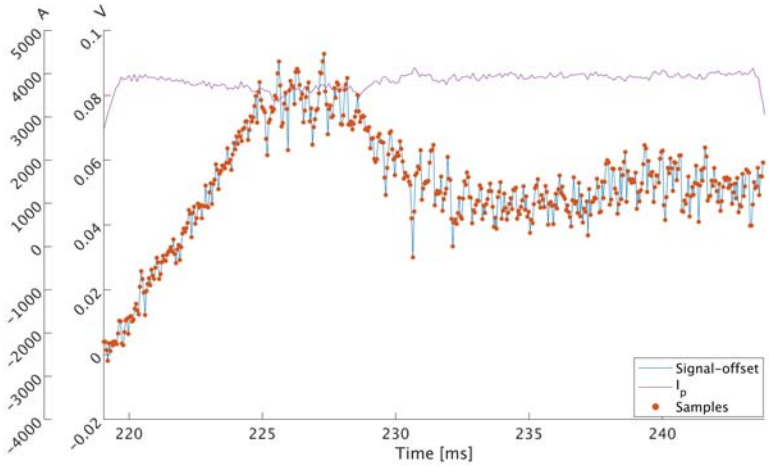

Figure 3.12: *Plot of the Plasma Current and HIBD Signal ch.29 , under-sampled ,* $f_{chopping} = 20$ *KHz,* $f_{low-pass} = 200$ *KHz,Time* [220 245]*, Shot* 47605

- Recover the $I_{j_{2+(det)}}$ intensity distribution in the detector row
- Estimate the current lost inside the EIM-CEA
- Compute the toroidal (z) shift on the Front detector

Interpolation

The first step to obtain an approximate value I_{SLIT} is to retrieve a 1D interpolated value I_{interp} in the y position that corresponds to the Slit,

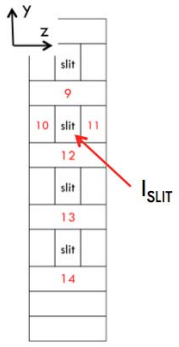

Figure 3.13: *Schematic representation of the Front detector (MCAD) and I_{SLIT} direction)*

Ch9, Ch.10 location (8 mm with respect to the reference system showed in fig. 3.14, from the current detected by the Front MCAD active cells ($I_{ch.9}$, $I_{ch.13}$, $I_{ch.12}$). The Matlab function used to get this interpolation is *interp1*. Two examples of the 1D interpolation output compared with the MCAD Signals ($I_{ch.9}$,$I_{ch.12}$ and $I_{ch.13}$) are showed in fig. 3.15, the plot show reasonable results with the I_{interp} values between $I_{ch.9}$ and $I_{ch.12}$ MCAD Signals amplitude.

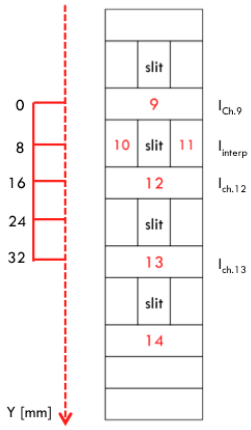

Figure 3.14: *Schematic representation of the Front detector (MCAD) and reference system*

An example of the 1D interpolation output compared with the MCAD Signals ($I_{ch.9}$,$I_{ch.12}$ and $I_{ch.13}$) is showed in fig. 3.15, the plot show reasonable results with the I_{interp} values between $I_{ch.9}$ and $I_{ch.12}$ MCAD Signals amplitude.

Once performed the 1D interpolation is possible to compute the 2D interpolation that is an approximate value of the current passing through the second slit I_{SLIT}, the equation used is:

$$I_{SLIT} = I_{interp} - (I_{ch.11} + I_{ch.10}) \tag{3.4}$$

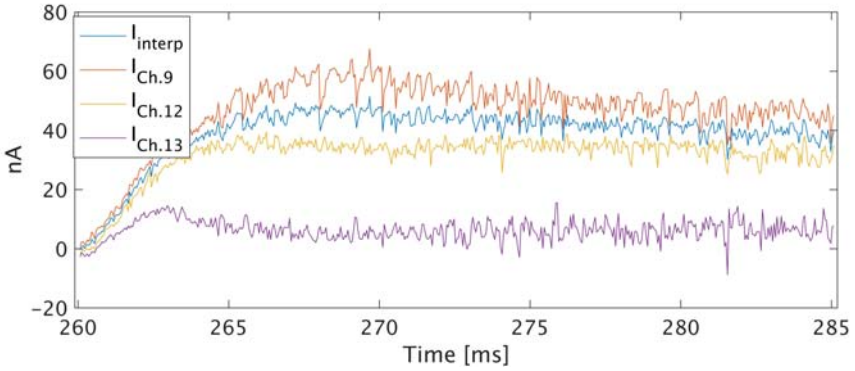

Figure 3.15: *Plot of the computed Signal* I_{SLIT} *and of the HIBD Signals ch.*9*,ch.*12*,ch.*13 *on Front MCAD, under-sampled ,*$f_{chopping} = 20$ *KHz,* $f_{low-pass} = 200$ *KHz, Shot* 47604*, Time* [260 285]

Comparing the total current detected by the Back MCAD $I_{Back} = I_{ch.21} + I_{ch.22}$ with the approximate value I_{SLIT} is possible to retrieve an estimation of the beam current lost at the entrance of the CEA. The same estimation could be performed with the Intermediate MCAD data, this detector in fact is located at the entrance of the CEA, but during the development of the thesis work the amplifiers were not working.

$$I_{EIM(\%)} = \frac{(I_{SLIT} - I_{Back})100}{I_{SLIT}} \tag{3.5}$$

The plots in fig. 3.16 and fig. 3.17 show two examples respectively referred to shot 47605 and 47604 of the I_{SLIT} and I_{BACK} values and the corresponding $I_{EIM(\%)}$ computed with eq. 3.5. On both cases the average over time of loss per-cent factor $I_{EIM(\%)}$ is within the range of $[45 - 50]$ %

3.3 SHIFT CROSS-CORRELATION

The third task of this thesis project is to demonstrate the low correlation (expected) between the B_p and V_p measurements cross-correlating the corresponding shifts. As explained in sections 2.2.3 and 2.2.3 there is a direct correlation between the measurements of the Poloidal Magnetic field B_p and of the Plasma potential V_p with the beam shifts on Front and Back MCADs, a schematic representation of the Shift directions are showed in fig. 3.18

B_p is correlated to the normalized Shift on toroidal direction (z) z_{Front} while V_p is correlated to the normalized shift on toroidal direction (x) z_{Back} .The two normalized Shift are computed by the equations 3.6

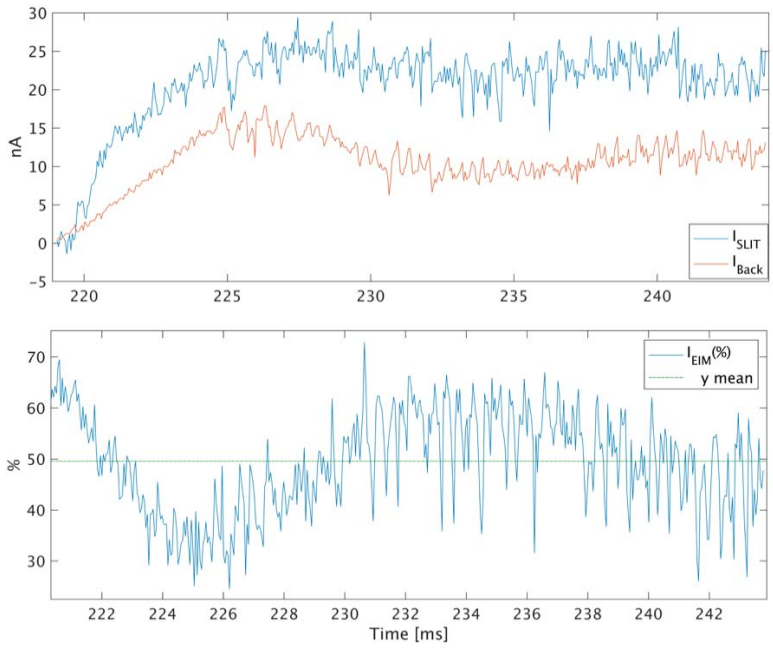

Figure 3.16: *Plot of the computed estimation* $I_{EIM(\%)}$*(lower picture) and of the HIBD Back Detector Signals , ch.*21 + *ch.*22*(higher picture),* $f_{chopping} = 20$ *KHz,* $f_{low-pass} = 200$ *KHz, Time* [220 245] *and Shot* 47605

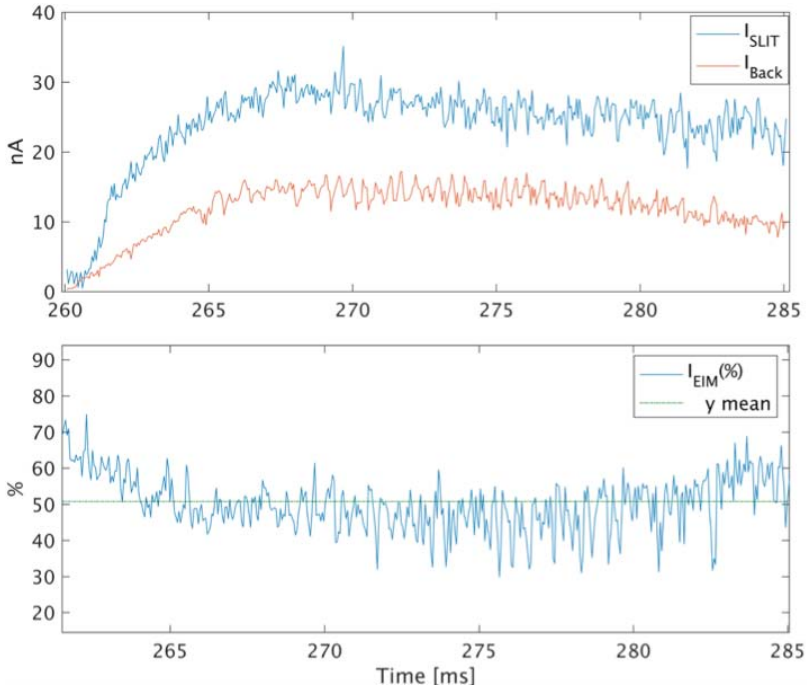

Figure 3.17: *Plot of the computed estimation* $I_{EIM(\%)}$*(lower picture) and of the HIBD Back Detector Signals ,ch.*21 + *ch.*22*(higher picture),*$f_{chopping} = 20$ *KHz,* $f_{low-pass} = 200$ *KHz, Time* [250 285] *and Shot* 47604

and 3.7. An example of z_{Front} and z_{Back} retrieved values are showed in fig. 3.19.

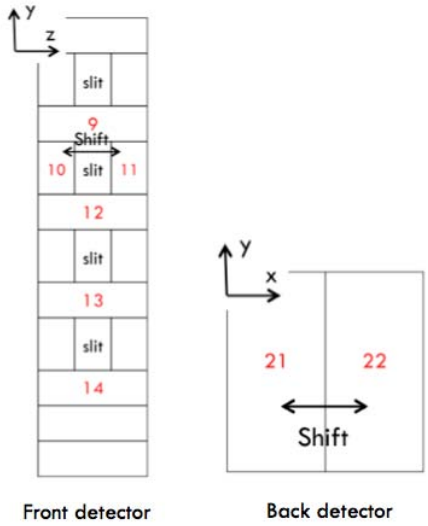

Figure 3.18: *Front MCAD and toroidal shift (z) direction schematic representation*

$$z_{Front} = \frac{I_{10} - I_{11}}{I_{10} + I_{11} + I_{SLIT}} \tag{3.6}$$

$$z_{Back} = \frac{I_{21} - I_{22}}{I_{21} + I_{22}} \tag{3.7}$$

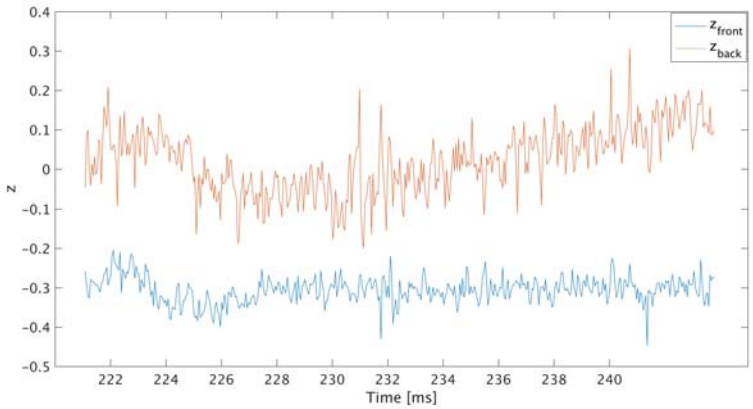

Figure 3.19: *Plot of the toroidal Shifts (Blue and red) under-sampled computed Signals,* $f_{chopping} = 20$ *KHz,* $f_{low-pass} = 200$ *KHz, Time* [220 245] *and Shot* 47605

3.3.1 *Cross-correlation in time*

A time-dependent cross-correlation was performed by performing several cross-correlations. The Cross-correlation is performed with respect

to time dividing into slices the two Signals with the time period of 4 ms (80 sample points) and cross-correlating each respective slice (wall slices) In order to increase the plot resolution a 40 % of slice overlapping has been applied:

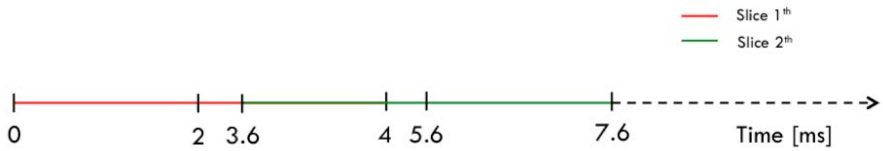

The results is a time-dependent cross- correlation, which is presented as a 3D and 2D plot. In fig. 3.20 are shown the output plots of the shots 47605 and 47604, where x-axis is the time that display the slice centre time instant, y-axis the slice time shift and z-axis are the normalized cross-correlation results $r_{xy}(m,t)$

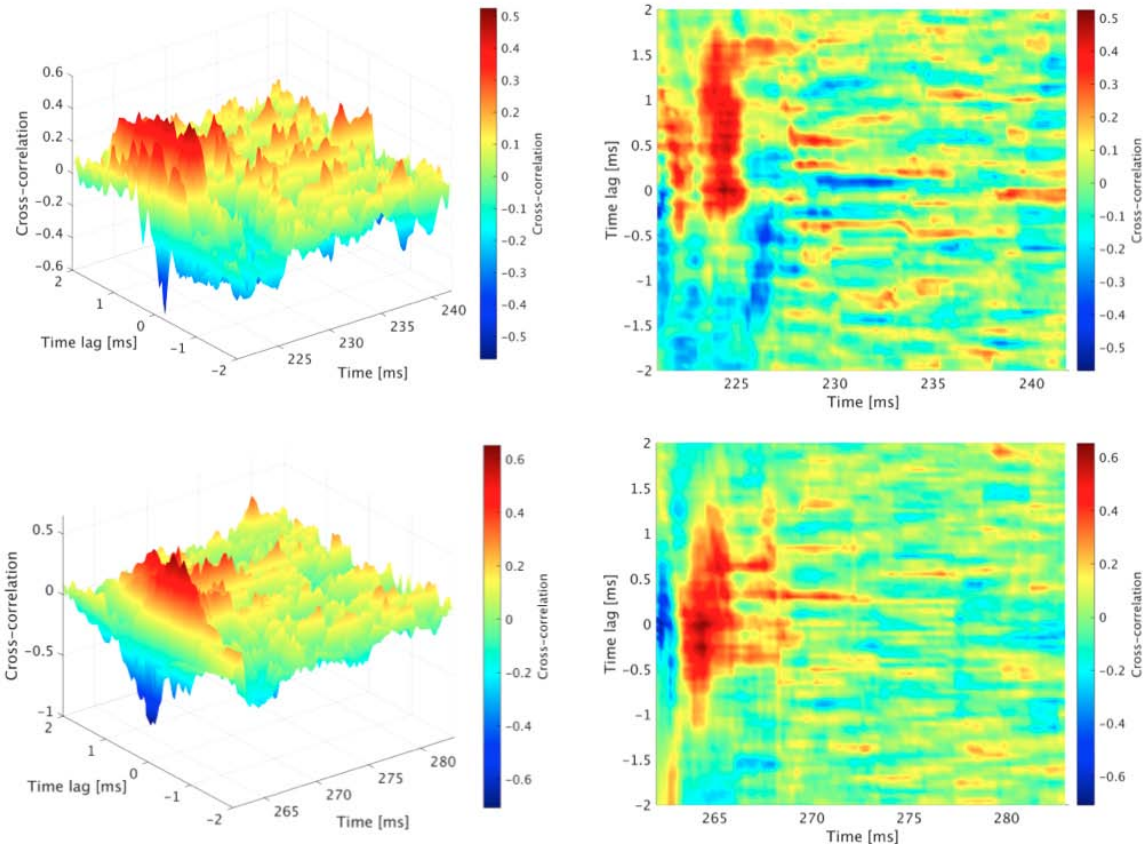

Figure 3.20: *Plot of the cross-correlation between Shifts under-sampled Signals in 3D (left) and 2D(right) view,* $f_{chopping} = 20$ *KHz,* $f_{low-pass} = 200$*, Shot* 47605 *(upper picture), Time* [260 285] *and Shot 47604 (lower pictures), Time* [220 245] *ms*

3.3.2 *Data Interpretation*

The 2D plot of the time-dependent cross - correlation compared with respect to the plasma discharge progression is shown in fig. 3.21. The normalized cross-correlation r_{xy} results between the two computed Shifts show low value (RMS) $\left[-0.2 < r_{xy} < 0.2\right]$ within the time range of plateau discharge ([225 245] ms in fig. 3.21) and Picks up to $r_{xy} = 0.5$ within the time range of discharge rump-up ([220 225] ms in fig. 3.21)

1. Poloidal Magnetic Field B_p variation that determinates a toroidal displacement of the beam position (see section 2.2.3)

2. Plasma Potential V_p variations that determinates a beam energy variation (δE) and as a consequence a Δr variation (see section 2.2.3)

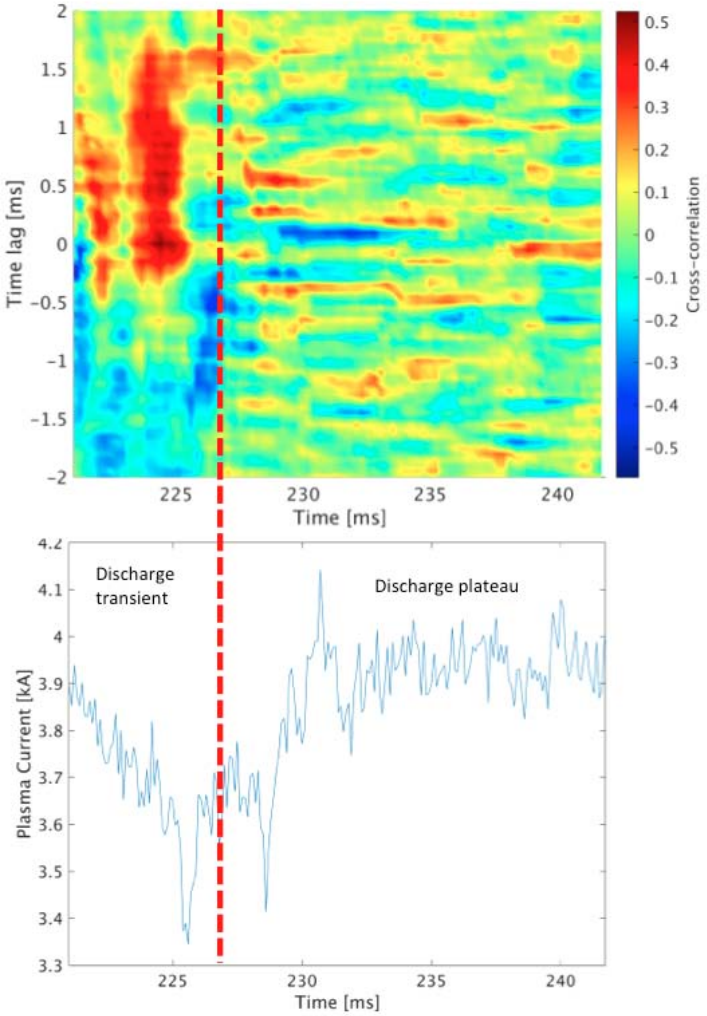

Figure 3.21: *Plot of the cross-correlation between Shifts under-sampled Signals in 2D view (upper picture),* $f_{chopping} = 20$ *KHz,* $f_{low-pass} = 200$ *and Plasma Current (lower picture), Time* [220 245] *ms, Shot* 47604

Up to 225 ms (part a)) there is a similar change of Vp and Bp. When current increases again to the same values (part b)) fig. 3.22 the cross correlation indicator shows very little CC meaning the measurements reflect a different evolution of the of Vp and Bp induced shifts, probably reflecting internal changes of the profiles compared to initial states of the discharge.

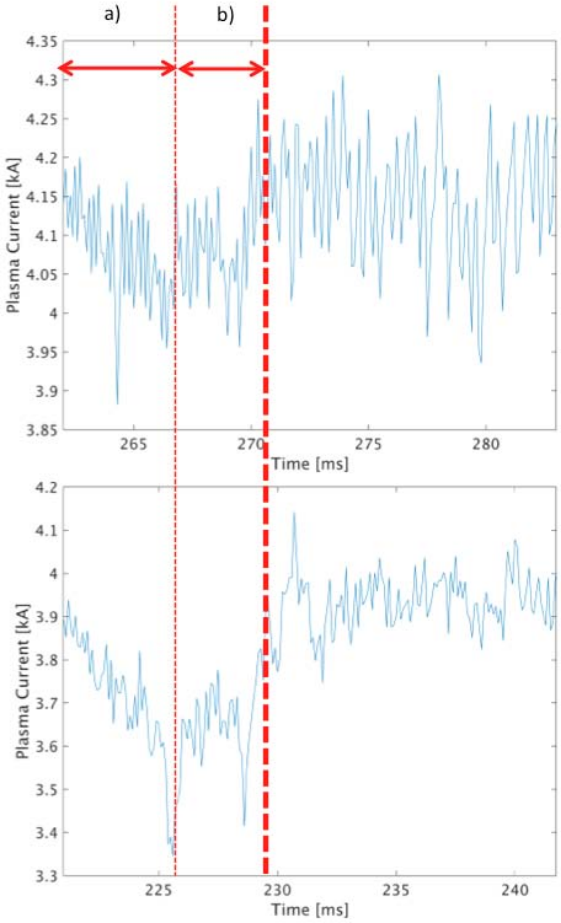

Figure 3.22: *Plot of the Plasma Current, Shot* 47604, *Time* [260 285] *ms (upper picture), Shot* 47605, *Time* [220 245] *ms (lower picture)*

The two different dynamics of plasma position displacement on the back and front MCADs respectively due to the B_p and V_p decreasing and increasing give a shift oscillation component visible in fig. 3.23 (lower pictures). The beam displacement causes an apparent correlation (0.5) between the two shift not related to the instantaneous fluctuation of the signal but rather to an independent but similar response to the change of plasma parameters (B_p and V_p).
During the discharge plateau, the plasma position is stabilized and the two shift measure the instant fluctuation of B_p and V_p without relevant interference as showed by the low correlation (RMS 0.2)

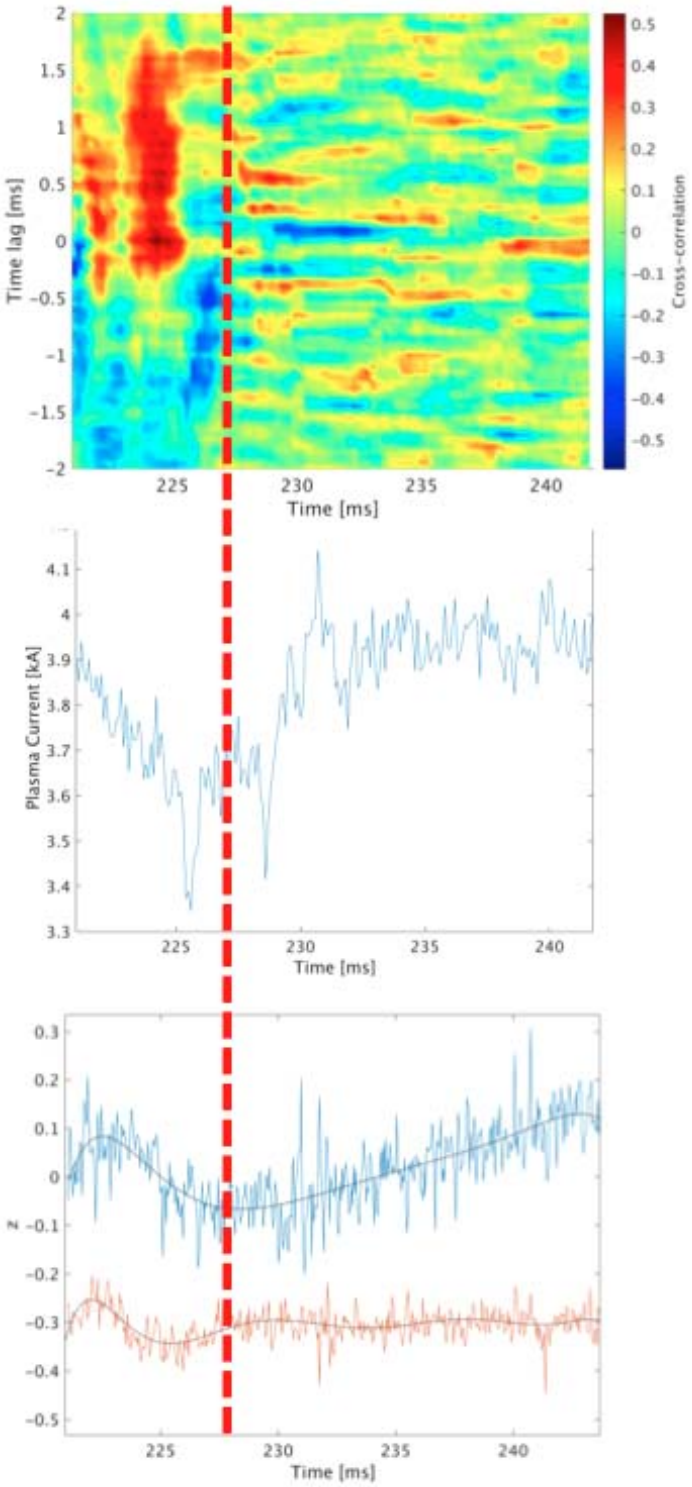

Figure 3.23: *Plot of the cross-correlation between Shifts under-sampled Signals in 2D view (upper pictures),* $f_{chopping} = 20$ *KHz,* $f_{low-pass} = 200$ *,Plasma Current (middle pictures) and Toroidal Shift on front and back MCADs; Shot* 47605, *Time* [220 245] *ms*

CONCLUSIONS

The output result observation leads to the conclusions that the comparison between the computed approximate value of the secondary beam current passing through the second slit I_{SLIT} and the current detected at the Back MCAD I_{Back} show an attenuation of the secondary beam current at the entrance of the CEA in the range of $[45 - 50\%]$ time average per-cent value.
The cross-correlation performed in time show a low correlation between the two toroidal shift (Back and Front MCADs) mean values $\left[-0.2 < r_{xy}(t) < 0.2\right]$ during the plasma current plateau time range, as expected. During discharge transient an higher apparent correlation (up to ± 0.5) is showed caused by a similar beam current position displacement due to two independent causes (B_p and V_p variation). As a consequence the experimental results show no relevant interference between B_p and V_p measurements respectively associated to Back and Front MCADs Shifts.

BIBLIOGRAPHY

[1] Andrea Pezzoli, Matteo Passoni, David Dellasega, and Carlo E Bottani. Tungsten-based coatings for magnetic fusion research: damage and hydrogen retention The Chair of the Doctoral Program: Year 2016-Cycle XXIX. *Politecnico di Milano*, 2016.

[2] H Fernandes, C Silva, J A C Cabral, and C A F Varandas. OV / P-08 20 years of ISTTOK tokamak scientific activity OV / P-08. *Associação Euratom/IST*, pages 1–7, 2010.

[3] Gonçalo Nuno, Cerqueira Olim, and Marote Quintal. Control of Nuclear Fusion Experiments. *IST*, 2014.

[4] J. A.C. Cabral, A. Malaquias, A. Praxedes, W. V. van Toledo, and C. A.F. Varandas. The Heavy Ion Beam Diagnostic for the Tokamak ISTTOK. *IEEE Transactions on Plasma Science*, 22(4):350–358, 1994.

[5] R. Sharma, I. S. Nedzelskiy, A. Malaquias, and R. B. Henriques. Design and optimization of the electrostatic input module for the ISTTOK Tokamak HIBD cylindrical energy analyzer. *Journal of Instrumentation*, 12(11), 2017.

[6] I. S. Nedzelskiy, A. Malaquias, R. Sharma, and R. Henriques. 90 cylindrical analyzer for the plasma potential fluctuations measurements by heavy ion beam diagnostic on the tokamak ISTTOK. *Fusion Engineering and Design*, 123:897–900, 2017.

[7] Caineng Zou, Qun Zhao, Guosheng Zhang, and Bo Xiong. Energy revolution: From a fossil energy era to a new energy era. *Natural Gas Industry*, 36(1):1–10, 2016.

[8] Francesco Romanelli. Fusion Electricity A roadmap to the realisation of fusion energy 28 European countries signed an agreement to work on an energy source for the future :. *Fusion Electricity - EFDA*, pages 1–75, 2012.

[9] Emelie Nilsson. Modelling of Lower Hybrid Current Drive in the Tore Supra Tokamak. *Chalmers University of Technology*, pages 1–56, 2012.

[10] H. Fernandes, C. A.F. Varandas, J. A.C. Cabral, H. Figueiredo, and R. Galvão. Engineering aspects of the ISTTOK operation in a multicycle alternating flat-top plasma current regime. *Fusion Engineering and Design*, 43(1):101–113, 1998.

[11] Ivo S. Carvalho, Paulo Duarte, Horácio Fernandes, Daniel F. Valcárcel, Pedro J. Carvalho, Carlos Silva, André S. Duarte, André Neto, Jorge Sousa, António J.N. Batista, and Bernardo B. Carvalho. ISTTOK control system upgrade. *Fusion Engineering and Design*, 88(6-8):1122–1126, 2013.

[12] Ivo S. Carvalho, Paulo Duarte, Horácio Fernandes, Daniel F. Valcárcel, Pedro J. Carvalho, Carlos Silva, André S. Duarte, André Neto, Jorge Sousa, António J.N. Batista, Tiago Hekkert, Bernardo B. Carvalho, and Rui B. Gomes. Real-time control for

long ohmic alternate current discharges. *Fusion Engineering and Design*, 89(5):576–581, 2014.

[13] J. A C Cabral, H. Fernandes, H. Figueiredo, and C. A F Varandas. Operation of the tokamak ISTTOK in a multicycle alternating flat-top plasma current regime. *Nuclear Fusion*, 37(11):1575–1581, 1997.

[14] Doctor Artur and Jorge Louzeiro. INSTITUTO SUPERIOR T ECNICO ISTTOK plasma characterization and control by the Heavy Ion Beam Diagnostic Rafael Bagagem Henriques. *Natural Gas Industry*, 1, 2019.

[15] Yu N. Dnestrovskij, A. V. Melnikov, L. I. Krupnik, and I. S. Nedzelskij. Development of Heavy Ion Beam Probe Diagnostics. *IEEE Transactions on Plasma Science*, 22(4):310–331, 1994.

[16] R. L. Hickok. A Short History of Heavy Ion Beam Probing. *IEEE Transactions on Plasma Science*, 22(4):287–290, 1994.

[17] A. Malaquias, I. S. Nedzelskii, C. A. F. Varandas, and J. A. C. Cabral. Evolution of the tokamak ISTTOK plasma density and electron temperature radial profiles determined by heavy ion beam probing. *Review of Scientific Instruments*, 70(1):947–950, 2002.